The Astronomical Journal, 154:5 (22pp), 2017 July https://doi.org/10.3847/1538-3881/aa71ef

Kepler Planet Masses and Eccentricities from TTV Analysis

Sam Hadden[1,2] and Yoram Lithwick[1,2]
[1] Department of Physics & Astronomy, Northwestern University, Evanston, IL 60208, USA
[2] Center for Interdisciplinary Exploration and Research in Astrophysics (CIERA), USA
Received 2016 November 9; revised 2017 January 30; accepted 2017 February 8; published 2017 June 9

Abstract

We conduct a uniform analysis of the transit timing variations (TTVs) of 145 planets from 55 *Kepler* multiplanet systems to infer planet masses and eccentricities. Eighty of these planets do not have previously reported mass and eccentricity measurements. We employ two complementary methods to fit TTVs: Markov chain Monte Carlo simulations based on *N*-body integration, and an analytic fitting approach. Mass measurements of 49 planets, including 12 without previously reported masses, meet our criterion for classification as robust. Using mass and radius measurements, we infer the masses of planets' gaseous envelopes for both our TTV sample and transiting planets with radial velocity observations. Insight from analytic TTV formulae allows us to partially circumvent degeneracies inherent to inferring eccentricities from TTV observations. We find that planet eccentricities are generally small, typically a few percent, but in many instances are nonzero.

Key words: planets and satellites: detection

Supporting material: figure set, machine-readable tables

1. Introduction

The *Kepler* mission's census of exoplanetary systems has provided us with a statistical picture of the properties of planetary systems (Borucki et al. 2010). Small planets with radii in the range $R_p = 1$–$4\ R_\oplus$ on short-period orbits, $P < 100$ days, are among the most abundant, occurring around roughly half of Sun-like stars (e.g., Fressin et al. 2013; Petigura et al. 2013). The distributions of planet sizes and periods measured by *Kepler* provide important constraints for theories of planet formation and evolution. Mass measurements, which constrain planets' compositions, and eccentricity measurements, which reveal the current dynamical states of planetary systems, are also essential clues for understanding formation and evolution processes.

The radial velocity (RV) method has provided the majority of exoplanet mass and eccentricity measurements to date (e.g., exoplanets.org; Wright et al. 2011). Mass measurements of transiting super-Earth and sub-Neptune planets are of particular interest given the ubiquity of such planets and their absence from our own solar system. Many sub-Jovian transiting planets have had their masses measured through RV follow-up (e.g., Bakos et al. 2010; Bordé et al. 2010; Borucki et al. 2010; Hartman et al. 2011; Gautier et al. 2012; Gilliland et al. 2013; Pepe et al. 2013; Alonso et al. 2014; Barros et al. 2014; Dumusque et al. 2014; Kostov et al. 2014; Marcy et al. 2014; Moutou et al. 2014; Dressing et al. 2015; Esteves et al. 2015; Gettel et al. 2016; Sinukoff et al. 2016). These efforts have yielded important constraints on the mass–radius relationship of super-Earth and sub-Neptune planets: Weiss & Marcy (2014) infer a mass–radius relationship of planets smaller than $4\ R_\oplus$ using available RV mass determinations, supplemented with a handful of masses determined from transit timing. Rogers (2015) uses the sample of *Kepler* planets with Keck HIRES RV follow-up to infer that planets transition from mainly rocky to volatile-rich compositions above a size of $1.6\ R_\oplus$. However, the RV method is of limited applicability to *Kepler*'s many sub-Neptune planets since the RVs induced by such planets often require intense follow-up efforts to detect. With a handful of exceptions, RV mass determinations of sub-Neptunes have been limited to planets with orbital periods shorter than 20 days.

The limitations of RV are even more acute for measuring sub-Neptunes' eccentricities since high signal-to-noise ratios are required to accurately infer eccentricities with RV (Shen & Turner 2008; Zakamska et al. 2011). Eccentricities of transiting planets can also be measured by modeling transit light curves. However, light-curve modeling yields useful constraints only in special circumstances: giant planets with large eccentricities (Dawson & Johnson 2012), planets with occultation detections (Shabram et al. 2016), or host stars with strong density constraints from asteroseismology (Kipping 2014). Statistical analyses of the transit durations of planets around well-characterized host stars have been used to constrain planet samples' overall eccentricity distributions (Van Eylen & Albrecht 2015; Xie et al. 2016), but inferring the eccentricities of individual sub-Neptune planets from light-curve modeling remains difficult.

Transit timing variations (TTVs) are a powerful tool for measuring masses and eccentricities in multiple-transiting systems (Agol et al. 2005; Holman 2005). The large TTV amplitudes induced in planets near mean motion resonances (MMRs) can probe the masses and eccentricities of small planets at relatively long orbital periods, which would otherwise be difficult or impossible to measure via the RV method. However, inverting TTVs to infer planet properties poses a difficult parameter inference problem: it requires fitting a large number of parameters, often with strong degeneracies, to noisy data. Statistical analyses of samples of TTV systems can overcome some of these difficulties (Wu & Lithwick 2013; Hadden & Lithwick 2014). Alternatively, the parameter inference challenge can be addressed with Markov chain Monte Carlo (MCMC) simulations when fitting TTVs of individual systems. MCMC is well suited for high-dimensional parameter inference problems and has been used frequently in TTV studies (e.g., Sanchis-Ojeda et al. 2012; Huber et al. 2013; Masuda et al. 2013; Schmitt et al. 2014; Jontof-Hutter et al. 2015, 2016; Hadden & Lithwick 2016; Mills et al. 2016).

While MCMC can efficiently sample planet masses and orbits consistent with TTV observations, interpreting MCMC results is often complicated by strong parameter correlations and sensitivity to priors. Analytic TTV formulae identify degeneracies inherent to inverting TTVs and aid the interpretation of N-body MCMC results. Components of the TTV signal responsible for mass and eccentricity constraints can be identified with analytic formulae and lend support to the robustness of N-body results to different prior assumptions.

In this paper we compute MCMC fits to the TTVs of 55 *Kepler* multiplanet systems exhibiting significant TTVs, 33 of which do not have N-body TTV fits reported previously in the literature. In addition, our work provides a uniform treatment of TTV systems that have previously been analyzed elsewhere. We complement our MCMC fits, which rely on N-body integrations, with an analytic approach to TTV modeling. The paper is organized as follows: We review analytic TTV formulae in Section 2 and describe our fitting methods in Section 3. Results of our fits are described in Section 4: Section 4.1 presents our mass and eccentricity measurements, and in Section 4.2 we provide a comparison with past results. We discuss our results in Section 5: in Section 5.1 we use planet radii and masses derived from our TTV fits to infer the masses of planets' gaseous envelopes, and in Section 5.2 we briefly discuss implications of the eccentricities inferred from TTVs. We conclude in Section 6.

2. Analytic TTV

2.1. The Analytic TTV Formula

A number of authors have derived analytic formulae to approximate TTVs using perturbative methods (e.g., Agol et al. 2005; Nesvorný & Morbidelli 2008; Nesvorný 2009; Lithwick et al. 2012; Deck & Agol 2015, 2016; Agol & Deck 2016; Hadden & Lithwick 2016; Nesvorný & Vokrouhlický 2016). Analytic formulae aid the interpretation of N-body fitting results by elucidating degeneracies and identifying TTV features that constrain planet masses and eccentricities. In this paper we apply the analytic formulae derived in Hadden & Lithwick (2016, hereafter Paper I) as part of our analysis of each system's TTVs. The main features of these formulae are summarized below.

For clarity, we focus our discussion on a planet near a j:$j-1$ first-order MMR with an exterior perturber. Other configurations are discussed in Section 2.3 The analytic formulae express a planet's TTV as a sum of harmonic terms:

$$\delta t(t) = \delta\hat{t}_{\mathcal{F}} e^{2\pi i t/P_{\rm sup}} + \delta\hat{t}_{\mathcal{S}} e^{4\pi i t/P_{\rm sup}} + \delta\hat{t}_{\mathcal{C}} \sum_{k=1,k\neq j}^{\infty} C_k e^{k(2\pi i t/P_{\rm syn})} + \text{c.c.}, \quad (1)$$

where the three successive terms are called "fundamental," "second-harmonic," and "chopping" TTVs, and "c.c." denotes complex conjugate. The frequencies of the harmonics are expressed in terms of the "super-period," $P_{\rm sup}$, and synodic period, $P_{\rm syn}$. These depend only on the period of the planet and its perturber and hence may be considered to be "known" for transiting planets. The dependence on masses and eccentricities is contained entirely in the amplitudes $\delta\hat{t}_{\mathcal{F}}$, $\delta\hat{t}_{\mathcal{S}}$, and $\delta\hat{t}_{\mathcal{C}}$. Since the first two of these are complex numbers and the third is real, there are in total five observables that can be used to infer masses and eccentricities. (The coefficients C_k depend only on the period ratio of the two planets.) The fundamental TTV is typically the dominant component. Its complex amplitude depends on mass and eccentricity and is given by

$$\delta\hat{t}_{\mathcal{F}} = \mu'(A + B\mathcal{Z}^*), \quad (2)$$

where A and B are coefficients that depend only on the planets' periods, μ' is the perturber's planet–star mass ratio, and

$$\mathcal{Z} \equiv \frac{f_{27} z + f_{31} z'}{\sqrt{f_{27}^2 + f_{31}^2}}, \quad (3)$$

$$\approx \frac{1}{\sqrt{2}}(z' - z). \quad (4)$$

where z and z' are the *free* complex eccentricities[3] of the inner and outer planet, and the f_i are coefficients that depend only on the planets' period ratio (see Paper I).

2.2. Degeneracies

In attempting to extract planet parameters from the dominant (fundamental) harmonic of the TTV, there are at least two kinds of degeneracies (Lithwick et al. 2012). The first is between the two planets' individual complex eccentricities—the *eccentricity–eccentricity degeneracy*. Since the fundamental TTV depends on the planets' eccentricities only through the single linear combination $\mathcal{Z}$, the z and z' of each planet are not separately measurable. This degeneracy persists even with the inclusion of the chopping and second-harmonic terms.

The second degeneracy is between μ' and $|\mathcal{Z}|$, which we call the *mass–eccentricity degeneracy*: a smaller μ' can be compensated for by a larger $|\mathcal{Z}|$ (Equation (2)). A modest uncertainty in $|\mathcal{Z}|$ will often result in a large uncertainty in μ' because typically $B \gg A$ in Equation (2).

The mass–eccentricity degeneracy can be broken if the chopping component can be resolved in the TTV signal (Nesvorný & Vokrouhlický 2014; Deck & Agol 2015). The chopping TTV is insensitive to eccentricities and provides a measurement of the perturbing planet's mass. In fact, the chopping TTV amplitude can simply be equated to the perturber's planet–star mass ratio,

$$\delta\hat{t}_{\mathcal{C}} = \mu', \quad (5)$$

with appropriate choice of scaling for the C_k coefficients in Equation (1). If a perturbing planet's mass can be measured from the chopping TTV, then the fundamental TTV amplitude gives the planets' combined eccentricity (Equation (2)).

The mass–eccentricity degeneracy may alternatively be broken by detecting the second-harmonic component, the amplitude of which is given by

$$\delta\hat{t}_{\mathcal{S}} = \mu'(D\mathcal{Z}^* + E\mathcal{Z}^{*2}), \quad (6)$$

with coefficients D and E depending only on planet periods.[4] Measuring both a planet's fundamental and second-harmonic

[3] A planet's total complex eccentricity, $ee^{i\varpi}$, is the sum of its free eccentricity plus a forced component induced by the forcing of perturbing companions. Forced components of the total eccentricity are typically much smaller than the free eccentricities we infer, so that the difference between free and total complex eccentricities is usually negligible.

[4] As shown in the Appendix of Paper I, the fact that Equation (6) depends on z and z' only through the combination $\mathcal{Z}$ is an approximation, albeit an excellent one. The approximation breaks down in the case of planets near the 2:1 MMR, allowing second-harmonic TTVs to constrain individual eccentricities.

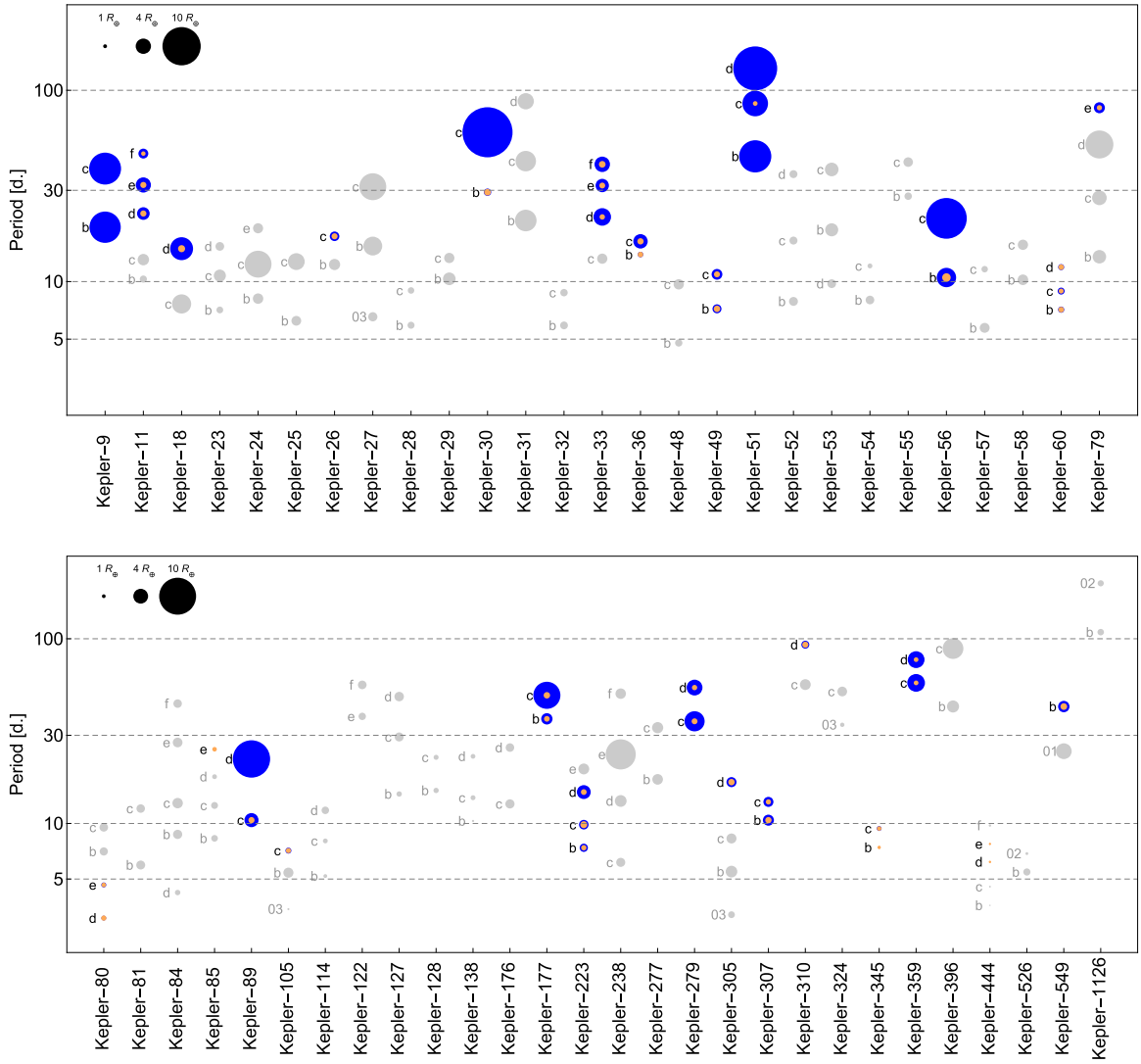

Figure 1. Multiplanet TTV systems fit in this paper. Planets in each system are plotted along the vertical axis according to their periods. The (outer) radii of the plotted circles are proportional to observed radii. The radii of planets with robust masses greater than 1 $M_\oplus$ and radii $R_p < 8\,R_\oplus$ are shown decomposed into an Earth-composition core (orange) and H/He envelope (blue) using the results of Section 5.1. Planets larger than $R_p > 8\,R_\oplus$ with robust masses are shown in blue without a core, and planets with robust masses smaller than 1 $M_\oplus$ are entirely orange. Planets that do not have robustly constrained masses are shown in gray.

TTV can break the degeneracy between mass and eccentricity since the functional dependence of each component on $\mathcal{Z}$ is different. Most of the TTV systems analyzed in this paper have small eccentricities so that we typically infer upper limits on combined eccentricity from the lack of substantial second-harmonic TTVs.

2.3. Other Configurations

With minor modifications, Equation (1) also describes the TTVs of planets subject to an interior perturber. Thus, breaking the mass–eccentricity degeneracy for one planet determines the pair's $\mathcal{Z}$ and thereby automatically breaks the degeneracy for both planets.

Equation (1) without the fundamental TTV term also describes the TTVs of planets near a j:$j-2$ second-order MMR. Proximity to a second-order resonance enhances the $\delta\hat{t}_{\mathcal{S}}$ term in Equation (1), which in this context we refer to as the "second-order resonance" component rather than a second-harmonic component. TTVs near second-order MMRs exhibit essentially the same mass–eccentricity and eccentricity–eccentricity degeneracies as planets near first-order MMRs, and the mass–eccentricity degeneracy can be broken by measuring a chopping component in either planet's TTV.

We find that, in practice, measuring (only) fundamental TTVs of three or more planets generally does not resolve any of the degeneracies inherent to the two-planet case.

3. TTV Fit Methods

We analyze TTVs of 145 planets from 55 different *Kepler* systems. Figure 1 shows the TTV systems fit in this paper. Our analysis is based on transit times computed by Rowe et al. (2015) from long-cadence *Kepler* data spanning Quarters 1–17. Each system is fit with both N-body MCMC simulations and the analytic TTV formulae. Systems are discussed individually in the Appendix. Results for their masses and eccentricities are summarized in Tables 1 and 2.

Our MCMC simulations sample the most likely planet masses and orbital elements of a multiple-transiting system given the planets' transit times by using N-body integrations.

Table 1
Masses from TTVs

Planet	Period (days)	Radius ($R_\oplus$)	Star Mass ($M_\odot$)	Mass (Default) ($M_\oplus$)	Density (Default) (g cm^{-3})	Mass (High Mass) ($M_\oplus$)	Density (High Mass) (g cm^{-3})	Reference
Kepler-9 b*	19.243	$8.2^{+1.0}_{-0.7}$	$1.0^{+0.1}_{-0.1}$	$43.5^{+2.7}_{-3.3}$	$0.4^{+0.1}_{-0.1}$	$43.4^{+2.7}_{-3.2}$	$0.4^{+0.1}_{-0.1}$	Ho10, Dr14, Bo14
Kepler-9 c*	38.969	$8.3^{+0.8}_{-0.9}$	...	$29.9^{+1.8}_{-2.3}$	$0.3^{+0.1}_{-0.1}$	$29.9^{+1.9}_{-2.2}$	$0.3^{+0.1}_{-0.1}$	Ho10, Dr14, Bo14
Kepler-11 b	10.304	$1.9^{+0.1}_{-0.1}$	$0.9^{+0.1}_{-0.1}$	$0.7^{+0.3}_{-0.2}$	$0.6^{+0.3}_{-0.2}$	$1.2^{+0.6}_{-0.5}$	$1.0^{+0.5}_{-0.5}$	Li11, M12, Li13, Bo14
Kepler-11 c	13.025	$3.0^{+0.2}_{-0.2}$	...	$1.8^{+0.9}_{-0.5}$	$0.4^{+0.2}_{-0.1}$	$3.4^{+1.4}_{-1.5}$	$0.7^{+0.4}_{-0.3}$	Li11, M12, Li13, Bo14
Kepler-11 d*	22.687	$3.3^{+0.2}_{-0.2}$	...	$6.8^{+0.7}_{-0.8}$	$1.0^{+0.2}_{-0.2}$	$6.9^{+0.8}_{-0.8}$	$1.0^{+0.3}_{-0.2}$	Li11, M12, Li13, Bo14
Kepler-11 e*	31.995	$4.0^{+0.2}_{-0.3}$	...	$6.7^{+1.2}_{-1.0}$	$0.6^{+0.2}_{-0.1}$	$7.2^{+1.1}_{-1.0}$	$0.7^{+0.1}_{-0.1}$	Li11, M12, Li13; Bo14
Kepler-11 f*	46.686	$2.6^{+0.2}_{-0.2}$	...	$1.7^{+0.5}_{-0.4}$	$0.5^{+0.2}_{-0.2}$	$1.9^{+0.5}_{-0.4}$	$0.6^{+0.2}_{-0.2}$	Li11, M12, Li13, Bo14
Kepler-18 c	7.642	$5.0^{+0.3}_{-0.3}$	$0.9^{+0.1}_{-0.02}$	$12.9^{+5.6}_{-6.6}$	$0.5^{+0.3}_{-0.3}$	$21.6^{+3.2}_{-4.0}$	$1.0^{+0.2}_{-0.3}$	Co11
Kepler-18 d*	14.859	$6.0^{+0.4}_{-0.4}$	...	$14.9^{+1.8}_{-4.2}$	$0.3^{+0.1}_{-0.1}$	$16.2^{+1.3}_{-1.5}$	$0.4^{+0.1}_{-0.1}$	Co11
Kepler-23 b	7.107	$1.8^{+0.1}_{-0.1}$	$1.0^{+0.1}_{-0.1}$	$1.3^{+1.3}_{-0.5}$	$1.2^{+1.4}_{-0.5}$	$4.7^{+1.9}_{-1.9}$	$4.2^{+2.3}_{-1.6}$	⋯
Kepler-23 c	10.742	$3.2^{+0.2}_{-0.2}$	...	$2.2^{+2.8}_{-0.9}$	$0.3^{+0.5}_{-0.1}$	$9.1^{+3.4}_{-3.9}$	$1.3^{+0.8}_{-0.4}$	⋯
Kepler-23 d	15.274	$2.3^{+0.1}_{-0.1}$	...	<2.4	<1.1	$4.9^{+3.6}_{-3.5}$	$2.1^{+1.8}_{-1.5}$	⋯

Notes. Values and uncertainties reflect the peak posterior probabilities and 68.3% credible regions. The peak posterior probabilities are computed by finding the maximum likelihood of a kernel density estimate computed from the posterior sample. Credible regions are so-called "highest posterior density intervals": the smallest parameter range containing 68.3% of the posterior sample. In columns (5)–(8), 68.3% upper limits are listed for planets with masses that are consistent with 0. Planets with robustly inferred masses are indicated with a "*" (see Section 3). References are listed in column (9) for planets with masses previously inferred from *N*-body TTV fits or RV observations. Planet radii, masses, and densities in columns (3), (5), (6), and (7) incorporate the following: planet–star mass ratios sampled from our MCMC posteriors, planet–star radius ratios from the light-curve fit posteriors of Rowe et al. (2015), and randomly generated samples of host star properties. For the latter, samples of host star radii, masses, and densities are generated based on values reported in the *Kepler* stellar Q1–17 data release DR25, hosted on the exoplanet archive. For each *Kepler* system, random samples of stellar mass, radius, and density are drawn from skew-normal distributions (Azzalini 1985), with scale and shape parameters chosen to match the reported $\pm 1\sigma$ error bars. For some planets, the Rowe et al. (2015) light-curve fit posteriors are missing or contain a large number of points with impact parameters $b > 1$ and are clearly pathological. The radii of these planets are computed using planet–star radius ratios from other sources as indicated.

[a] Planet–star radius ratio from Borucki et al. (2011).
[b] Planet–star radius ratio from Fabrycky et al. (2012).
[c] Planet–star radius ratio from Masuda (2014).
[d] Planet–star radius ratio from Steffen et al. (2013).
[e] Planet–star radius ratio from Mills et al. (2016).
[f] Planet–star radius ratio from Rowe et al. (2014).
[g] Planet–star radius ratio from *Kepler* KOI Q1–17 data release DR24, hosted on the Exoplanet Archive.

(This table is available in its entirety in machine-readable form.)

Specifically, for a system of N planets our MCMC samples the posterior distribution of each planet's planet-to-star mass ratio, μ_i, eccentricity vector components $h_i \equiv e_i \cos(\varpi_i)$ and $k_i \equiv e_i \sin(\varpi_i)$, initial osculating period P_i, and time of first transit T_i, where $i = 1, 2, \ldots, N$. The complete details of our MCMC implementation are given in Paper I.

As in Paper I, in order to assess how robustly planet properties are constrained by the TTVs, we run two MCMC simulations for each system we fit with two different priors for masses and eccentricities. Our first (default) prior is logarithmic in planet masses ($dP/dM \propto M^{-1}$) and uniform in eccentricities ($dP/de \propto$ const.). Our second (high-mass) prior is uniform in planet masses ($dP/dM \propto$ const.) and logarithmic in eccentricity ($dP/de \propto e^{-1}$). (Uniform sampling in the variables $e\cos(\varpi)$ and $e\sin(\varpi)$ results in $dP/de \propto e$, so the default and high-mass prior probabilities are implemented by including a factor of $1/e$ and $1/e^2$, respectively, when computing the prior probability.) We will refer to the posterior distributions computed with the respective priors as the default and high-mass posteriors. Inferred planet masses are classified as "robust" if the 1σ credible region of the default posterior excludes $\mu = 0$ and includes the peak of the high-mass posterior. Masses of 49 of the 145 planets are classified as robust. Twelve planets with robust masses do not have *N*-body fits previously reported in the literature.

We have chosen our two MCMC priors to weight toward opposite extremes of the mass–eccentricity degeneracy in order to assess the significance of this degeneracy in each system. Additionally, both priors are chosen to be "uninformative" or broad and do not rely on any theoretical predictions for planet compositions or eccentricities. Aside from these considerations, our adopted priors are arbitrary, and any number of other priors could be reasonably advocated.[5] It is possible that a different choice of priors could affect the inferred masses and eccentricities significantly. Instead of exploring a wide variety of priors with

[5] The interested reader can easily explore other priors via weighted resampling of the posterior samples. As a possible extension to this work, the posterior samples can be incorporated in the hierarchical modeling approach described by Hogg et al. (2010) to infer a prior (see also Rogers 2015). Together, the default and high-mass posteriors provide samples over a broad range of parameter space, as required by this method. Our posterior samples are available online (doi:10.5281/zenodo.162965).

Table 2
Combined Eccentricities of Adjacent TTV Planet Pairs

Planet Pair	Resonance	Δ	$\lvert\mathcal{Z}\rvert$ (Default)	$\mathcal{Z}_{\rm proj}$ (Default)	$\lvert\mathcal{Z}\rvert$ (High Mass)	$\mathcal{Z}_{\rm proj}$ (High Mass)
Kepler-9 b/c	2:1	0.0126	$0.083^{+0.001}_{-0.001}$	$0.083^{+0.001}_{-0.001}$	$0.083^{+0.001}_{-0.001}$	$0.083^{+0.001}_{-0.001}$
Kepler-11 b/c	5:4	0.0113	$0.028^{+0.006}_{-0.01}$	$0.028^{+0.006}_{-0.01}$	$0.01^{+0.008}_{-0.004}$	$0.01^{+0.008}_{-0.004}$
Kepler-11 c/d	5:3	0.0451	$0.013^{+0.015}_{-0.009}$	$0.001^{+0.023}_{-0.008}$	$0.001^{+0.008}_{-0.001}$	$0.00^{+0.009}_{-0.002}$
Kepler-11 d/e	7:5	0.0074	$0.009^{+0.001}_{-0.001}$	$0.009^{+0.001}_{-0.002}$	$0.009^{+0.001}_{-0.001}$	$0.009^{+0.002}_{-0.001}$
Kepler-11 e/f	3:2	−0.0272	$0.018^{+0.005}_{-0.004}$	$0.018^{+0.006}_{-0.004}$	$0.016^{+0.005}_{-0.004}$	$0.016^{+0.004}_{-0.004}$
Kepler-18 c/d	2:1	−0.0278	$0.001^{+0.005}_{-0.001}$	$0.001^{+0.006}_{-0.002}$	$0.002^{+0.0004}_{-0.001}$	$0.002^{+0.001}_{-0.001}$
Kepler-23 b/c	3:2	0.0077	$0.017^{+0.026}_{-0.006}$	$0.025^{+0.018}_{-0.013}$	$0.011^{+0.005}_{-0.003}$	$0.011^{+0.005}_{-0.003}$
Kepler-23 c/d	7:5	0.0156	$0.021^{+0.013}_{-0.014}$	$0.002^{+0.022}_{-0.018}$	$0.009^{+0.003}_{-0.009}$	$0.009^{+0.004}_{-0.011}$
Kepler-24 b/c	3:2	0.0095	$0.035^{+0.025}_{-0.014}$	$0.035^{+0.025}_{-0.014}$	$0.014^{+0.006}_{-0.004}$	$0.014^{+0.006}_{-0.004}$
Kepler-24 c/e	3:2	0.0269	$0.038^{+0.014}_{-0.018}$	$0.037^{+0.013}_{-0.024}$	$0.006^{+0.006}_{-0.006}$	$0.001^{+0.011}_{-0.001}$
Kepler-25 b/c	2:1	0.0195	$0.009^{+0.043}_{-0.008}$	$0.009^{+0.044}_{-0.008}$	$0.002^{+0.005}_{-0.001}$	$0.003^{+0.004}_{-0.003}$
Kepler-26 b/c	7:5	0.0032	$0.013^{+0.001}_{-0.001}$	$0.013^{+0.001}_{-0.001}$	$0.01^{+0.001}_{-0.001}$	$0.01^{+0.001}_{-0.001}$
Kepler-27 03/b	2:1	0.1713	$0.009^{+0.082}_{-0.008}$	$-0.006^{+0.071}_{-0.033}$	$0.006^{+0.003}_{-0.002}$	$0.005^{+0.003}_{-0.003}$
Kepler-27 b/c	2:1	0.0215	$0.034^{+0.022}_{-0.013}$	$0.034^{+0.022}_{-0.012}$	$0.019^{+0.007}_{-0.005}$	$0.02^{+0.007}_{-0.005}$
Kepler-28 b/c	3:2	0.0132	$0.038^{+0.017}_{-0.019}$	$0.038^{+0.018}_{-0.018}$	$0.005^{+0.012}_{-0.001}$	$0.008^{+0.009}_{-0.005}$
Kepler-29 b/c	9:7	−0.0005	$0.014^{+0.014}_{-0.003}$	$0.013^{+0.014}_{-0.003}$	$0.012^{+0.002}_{-0.001}$	$0.012^{+0.002}_{-0.001}$
Kepler-30 b/c	2:1	0.0287	$0.039^{+0.0003}_{-0.0003}$	$0.039^{+0.0003}_{-0.0003}$	$0.039^{+0.0003}_{-0.0003}$	$0.039^{+0.0003}_{-0.0003}$
Kepler-31 b/c	2:1	0.0219	$0.008^{+0.082}_{-0.005}$	$0.01^{+0.08}_{-0.009}$	$0.005^{+0.004}_{-0.001}$	$0.005^{+0.003}_{-0.002}$
Kepler-31 c/d	2:1	0.0279	$0.007^{+0.024}_{-0.005}$	$0.004^{+0.024}_{-0.005}$	$0.001^{+0.003}_{-0.001}$	$0.001^{+0.003}_{-0.001}$
Kepler-32 b/c	3:2	−0.0113	$0.096^{+0.011}_{-0.043}$	$0.094^{+0.01}_{-0.044}$	$0.004^{+0.004}_{-0.001}$	$0.004^{+0.004}_{-0.001}$
Kepler-33 c/d	5:3	−0.0084	$0.029^{+0.014}_{-0.015}$	$0.024^{+0.021}_{-0.018}$	$0.016^{+0.009}_{-0.008}$	$0.016^{+0.009}_{-0.01}$
Kepler-33 d/e	3:2	−0.0269	$0.008^{+0.004}_{-0.004}$	$0.007^{+0.005}_{-0.003}$	$0.009^{+0.003}_{-0.004}$	$0.008^{+0.004}_{-0.004}$
Kepler-33 e/f	9:7	0.004	$0.006^{+0.002}_{-0.002}$	$0.006^{+0.002}_{-0.002}$	$0.006^{+0.002}_{-0.002}$	$0.006^{+0.002}_{-0.003}$
Kepler-36 b/c	7:6	0.0048	$0.02^{+0.0004}_{-0.0005}$	$0.02^{+0.0005}_{-0.0004}$	$0.02^{+0.0003}_{-0.0003}$	$0.02^{+0.0003}_{-0.0004}$
Kepler-48 b/c	2:1	0.0123	$0.003^{+0.16}_{-0.003}$	$0.08^{+0.074}_{-0.082}$	$0.001^{+0.001}_{-0.001}$	$0.0004^{+0.0005}_{-0.0005}$
Kepler-49 b/c	3:2	0.0099	$0.003^{+0.001}_{-0.0004}$	$0.003^{+0.001}_{-0.001}$	$0.004^{+0.0004}_{-0.0004}$	$0.004^{+0.0004}_{-0.001}$
Kepler-51 b/c	2:1	−0.0553	$0.041^{+0.014}_{-0.011}$	$0.041^{+0.014}_{-0.011}$	$0.033^{+0.012}_{-0.009}$	$0.033^{+0.012}_{-0.009}$
Kepler-51 c/d	3:2	0.0172	$0.004^{+0.002}_{-0.001}$	$0.004^{+0.002}_{-0.002}$	$0.004^{+0.001}_{-0.002}$	$0.004^{+0.001}_{-0.002}$
Kepler-52 b/c	2:1	0.04	$0.151^{+0.091}_{-0.053}$	$0.154^{+0.084}_{-0.056}$	$0.066^{+0.029}_{-0.019}$	$0.066^{+0.029}_{-0.019}$
Kepler-52 c/d	2:1	0.1122	$0.129^{+0.051}_{-0.052}$	$0.115^{+0.06}_{-0.043}$	$0.056^{+0.026}_{-0.026}$	$0.052^{+0.028}_{-0.025}$
Kepler-53 b/c	2:1	0.0338	$0.133^{+0.042}_{-0.062}$	$0.123^{+0.049}_{-0.055}$	$0.017^{+0.009}_{-0.005}$	$0.018^{+0.007}_{-0.006}$
Kepler-53 d/b	2:1	−0.0438	$0.055^{+0.052}_{-0.039}$	$0.043^{+0.046}_{-0.073}$	$0.007^{+0.008}_{-0.005}$	$0.005^{+0.007}_{-0.005}$
Kepler-54 b/c	3:2	0.0046	$0.016^{+0.019}_{-0.005}$	$0.016^{+0.019}_{-0.005}$	$0.011^{+0.005}_{-0.002}$	$0.011^{+0.005}_{-0.002}$
Kepler-55 b/c	3:2	0.005	$0.036^{+0.02}_{-0.023}$	$0.037^{+0.019}_{-0.024}$	$0.002^{+0.007}_{-0.001}$	$0.005^{+0.006}_{-0.005}$
Kepler-56 b/c	2:1	0.0192	$0.03^{+0.008}_{-0.004}$	$0.03^{+0.008}_{-0.005}$	$0.028^{+0.004}_{-0.003}$	$0.028^{+0.004}_{-0.003}$
Kepler-57 b/c	2:1	0.0131	$0.024^{+0.076}_{-0.012}$	$0.023^{+0.075}_{-0.015}$	$0.016^{+0.009}_{-0.004}$	$0.016^{+0.008}_{-0.004}$
Kepler-58 b/c	3:2	0.016	$0.067^{+0.023}_{-0.027}$	$0.066^{+0.023}_{-0.027}$	$0.009^{+0.011}_{-0.003}$	$0.009^{+0.011}_{-0.003}$
Kepler-60 b/c	5:4	0.0003	$0.03^{+0.004}_{-0.003}$	$0.03^{+0.004}_{-0.004}$	$0.026^{+0.002}_{-0.002}$	$0.026^{+0.002}_{-0.002}$
Kepler-60 c/d	4:3	0.0006	$0.072^{+0.008}_{-0.007}$	$0.072^{+0.008}_{-0.007}$	$0.007^{+0.002}_{-0.002}$	$0.007^{+0.002}_{-0.002}$
Kepler-79 b/c	2:1	0.0161	$0.007^{+0.008}_{-0.003}$	$0.008^{+0.007}_{-0.005}$	$0.002^{+0.002}_{-0.0005}$	$0.003^{+0.002}_{-0.001}$
Kepler-79 c/d	2:1	−0.0495	$0.02^{+0.015}_{-0.012}$	$0.018^{+0.016}_{-0.011}$	$0.005^{+0.005}_{-0.003}$	$0.005^{+0.005}_{-0.004}$
Kepler-79 d/e	3:2	0.0375	$0.013^{+0.007}_{-0.005}$	$0.013^{+0.007}_{-0.006}$	$0.009^{+0.005}_{-0.004}$	$0.009^{+0.005}_{-0.004}$
Kepler-80 b/c	4:3	0.0124	$0.009^{+0.009}_{-0.005}$	$0.008^{+0.009}_{-0.005}$	$0.004^{+0.004}_{-0.002}$	$0.004^{+0.004}_{-0.002}$
Kepler-80 d/e	3:2	0.0081	$0.004^{+0.002}_{-0.001}$	$0.004^{+0.002}_{-0.002}$	$0.004^{+0.001}_{-0.002}$	$0.004^{+0.001}_{-0.002}$
Kepler-80 e/b	3:2	0.0123	$0.002^{+0.003}_{-0.001}$	$0.001^{+0.004}_{-0.002}$	$0.002^{+0.002}_{-0.001}$	$0.002^{+0.002}_{-0.001}$
Kepler-81 b/c	2:1	0.0109	$0.007^{+0.135}_{-0.005}$	$0.004^{+0.124}_{-0.005}$	$0.004^{+0.002}_{-0.001}$	$0.004^{+0.002}_{-0.001}$
Kepler-84 b/c	3:2	−0.0157	$0.008^{+0.029}_{-0.006}$	$0.008^{+0.028}_{-0.007}$	$0.003^{+0.004}_{-0.002}$	$0.003^{+0.004}_{-0.003}$
Kepler-84 c/e	2:1	0.0648	$0.019^{+0.036}_{-0.015}$	$0.018^{+0.034}_{-0.019}$	$0.009^{+0.007}_{-0.005}$	$0.009^{+0.007}_{-0.004}$
Kepler-84 d/b	2:1	0.0328	$0.005^{+0.011}_{-0.005}$	$-0.0002^{+0.013}_{-0.005}$	$0.001^{+0.005}_{-0.001}$	$-0.001^{+0.006}_{-0.002}$
Kepler-84 e/f	5:3	−0.0257	$0.01^{+0.015}_{-0.008}$	$0.005^{+0.017}_{-0.017}$	$0.002^{+0.007}_{-0.001}$	$0.001^{+0.007}_{-0.003}$
Kepler-85 b/c	3:2	0.0045	$0.002^{+0.014}_{-0.001}$	$0.002^{+0.014}_{-0.002}$	$0.001^{+0.001}_{-0.0004}$	$0.001^{+0.001}_{-0.001}$
Kepler-85 c/d	7:5	0.0225	$0.016^{+0.013}_{-0.011}$	$0.005^{+0.02}_{-0.008}$	$0.006^{+0.004}_{-0.004}$	$0.006^{+0.003}_{-0.006}$
Kepler-85 d/e	7:5	0.0054	$0.016^{+0.018}_{-0.012}$	$0.001^{+0.03}_{-0.01}$	$0.001^{+0.009}_{-0.001}$	$0.0002^{+0.007}_{-0.003}$
Kepler-89 c/d	2:1	0.0717	$0.015^{+0.005}_{-0.003}$	$0.015^{+0.005}_{-0.003}$	$0.014^{+0.003}_{-0.002}$	$0.014^{+0.003}_{-0.002}$
Kepler-105 03/b	3:2	0.0501	$0.035^{+0.018}_{-0.02}$	$0.027^{+0.016}_{-0.015}$	$0.011^{+0.011}_{-0.007}$	$0.008^{+0.011}_{-0.005}$
Kepler-105 b/c	4:3	−0.0125	$0.01^{+0.002}_{-0.002}$	$0.01^{+0.003}_{-0.002}$	$0.01^{+0.002}_{-0.001}$	$0.01^{+0.002}_{-0.001}$
Kepler-114 b/c	3:2	0.0332	$0.011^{+0.03}_{-0.009}$	$0.007^{+0.03}_{-0.014}$	$0.001^{+0.005}_{-0.001}$	$0.001^{+0.004}_{-0.003}$

Table 2
(Continued)

Planet Pair	Resonance	Δ	$\lvert\mathcal{Z}\rvert$ (Default)	$\mathcal{Z}_{\rm proj}$ (Default)	$\lvert\mathcal{Z}\rvert$ (High Mass)	$\mathcal{Z}_{\rm proj}$ (High Mass)
Kepler-114 c/d	3:2	−0.0237	$0.015^{+0.02}_{-0.009}$	$0.015^{+0.019}_{-0.01}$	$0.002^{+0.004}_{-0.002}$	$0.0001^{+0.005}_{-0.001}$
Kepler-122 e/f	3:2	−0.0129	$0.033^{+0.015}_{-0.018}$	$0.028^{+0.023}_{-0.012}$	$0.017^{+0.009}_{-0.005}$	$0.017^{+0.009}_{-0.005}$
Kepler-127 b/c	2:1	0.0181	$0.027^{+0.038}_{-0.012}$	$0.027^{+0.037}_{-0.011}$	$0.017^{+0.007}_{-0.006}$	$0.017^{+0.007}_{-0.006}$
Kepler-127 c/d	5:3	−0.0073	$0.023^{+0.008}_{-0.005}$	$0.023^{+0.008}_{-0.004}$	$0.02^{+0.003}_{-0.002}$	$0.02^{+0.003}_{-0.003}$
Kepler-128 b/c	3:2	0.0075	$0.084^{+0.031}_{-0.033}$	$0.088^{+0.025}_{-0.037}$	$0.008^{+0.014}_{-0.003}$	$0.008^{+0.014}_{-0.003}$
Kepler-138 b/c	4:3	0.0022	$0.006^{+0.004}_{-0.004}$	$0.006^{+0.004}_{-0.004}$	$0.001^{+0.001}_{-0.0003}$	$0.001^{+0.001}_{-0.001}$
Kepler-138 c/d	5:3	0.0052	$0.08^{+0.022}_{-0.021}$	$0.084^{+0.02}_{-0.023}$	$0.035^{+0.011}_{-0.008}$	$0.035^{+0.011}_{-0.009}$
Kepler-176 c/d	2:1	0.0092	$0.13^{+0.113}_{-0.125}$	$0.018^{+0.215}_{-0.014}$	$0.004^{+0.004}_{-0.002}$	$0.004^{+0.004}_{-0.002}$
Kepler-177 b/c	4:3	0.0056	$0.002^{+0.0002}_{-0.0003}$	$0.002^{+0.0002}_{-0.0003}$	$0.002^{+0.0002}_{-0.0002}$	$0.002^{+0.0002}_{-0.0002}$
Kepler-223 b/c	4:3	0.0002	$0.073^{+0.014}_{-0.014}$	$0.072^{+0.015}_{-0.013}$	$0.071^{+0.016}_{-0.013}$	$0.071^{+0.016}_{-0.013}$
Kepler-223 c/d	3:2	0.001	$0.003^{+0.004}_{-0.002}$	$0.002^{+0.003}_{-0.003}$	$0.005^{+0.006}_{-0.003}$	$0.005^{+0.006}_{-0.005}$
Kepler-223 d/e	4:3	0.0005	$0.021^{+0.01}_{-0.008}$	$0.021^{+0.01}_{-0.01}$	$0.023^{+0.007}_{-0.005}$	$0.022^{+0.008}_{-0.005}$
Kepler-238 c/d	2:1	0.0749	$0.012^{+0.061}_{-0.012}$	$0.003^{+0.068}_{-0.028}$	$0.012^{+0.014}_{-0.012}$	$0.01^{+0.016}_{-0.012}$
Kepler-238 d/e	5:3	0.0724	$0.037^{+0.025}_{-0.027}$	$0.013^{+0.041}_{-0.024}$	$0.001^{+0.015}_{-0.001}$	$0.0001^{+0.011}_{-0.007}$
Kepler-238 e/f	2:1	0.0663	$0.007^{+0.032}_{-0.007}$	$0.013^{+0.029}_{-0.022}$	$0.001^{+0.006}_{-0.001}$	$0.0003^{+0.006}_{-0.004}$
Kepler-277 b/c	2:1	−0.0474	$0.259^{+0.06}_{-0.173}$	$0.118^{+0.179}_{-0.053}$	$0.006^{+0.006}_{-0.005}$	$0.002^{+0.009}_{-0.005}$
Kepler-279 c/d	3:2	0.0151	$0.056^{+0.009}_{-0.009}$	$0.056^{+0.009}_{-0.009}$	$0.051^{+0.008}_{-0.01}$	$0.051^{+0.008}_{-0.009}$
Kepler-305 03/b	5:3	0.0271	$0.015^{+0.027}_{-0.012}$	$0.003^{+0.025}_{-0.019}$	$0.002^{+0.007}_{-0.002}$	$0.002^{+0.004}_{-0.007}$
Kepler-305 b/c	3:2	0.0073	$0.006^{+0.006}_{-0.003}$	$0.006^{+0.006}_{-0.003}$	$0.003^{+0.002}_{-0.001}$	$0.003^{+0.002}_{-0.001}$
Kepler-305 c/d	2:1	0.0095	$0.006^{+0.003}_{-0.002}$	$0.005^{+0.004}_{-0.002}$	$0.007^{+0.002}_{-0.002}$	$0.008^{+0.002}_{-0.003}$
Kepler-307 b/c	5:4	0.005	$0.003^{+0.0002}_{-0.0002}$	$0.003^{+0.0002}_{-0.0002}$	$0.003^{+0.0001}_{-0.0001}$	$0.003^{+0.0001}_{-0.0001}$
Kepler-310 c/d	5:3	−0.0133	$0.026^{+0.008}_{-0.014}$	$0.026^{+0.006}_{-0.035}$	$0.017^{+0.012}_{-0.008}$	$0.008^{+0.005}_{-0.005}$
Kepler-324 03/c	3:2	0.0097	$0.019^{+0.019}_{-0.008}$	$0.019^{+0.02}_{-0.009}$	$0.009^{+0.006}_{-0.002}$	$0.009^{+0.006}_{-0.002}$
Kepler-345 b/c	5:4	0.0127	$0.024^{+0.005}_{-0.005}$	$0.025^{+0.004}_{-0.005}$	$0.007^{+0.016}_{-0.002}$	$0.007^{+0.016}_{-0.002}$
Kepler-359 c/d	4:3	0.0021	$0.007^{+0.011}_{-0.004}$	$0.005^{+0.007}_{-0.005}$	$0.006^{+0.005}_{-0.003}$	$0.006^{+0.004}_{-0.006}$
Kepler-396 b/c	2:1	0.0293	$0.229^{+0.113}_{-0.072}$	$0.244^{+0.097}_{-0.087}$	$0.088^{+0.045}_{-0.029}$	$0.089^{+0.049}_{-0.025}$
Kepler-444 b/c	5:4	0.0102	$0.003^{+0.008}_{-0.002}$	$0.00^{+0.009}_{-0.003}$	$0.001^{+0.003}_{-0.001}$	$0.00^{+0.003}_{-0.002}$
Kepler-444 c/d	4:3	0.0212	$0.003^{+0.011}_{-0.002}$	$0.0004^{+0.009}_{-0.007}$	$0.002^{+0.002}_{-0.002}$	$0.001^{+0.002}_{-0.003}$
Kepler-444 d/e	5:4	0.0009	$0.001^{+0.0004}_{-0.0002}$	$0.001^{+0.0005}_{-0.0002}$	$0.001^{+0.0002}_{-0.0002}$	$0.001^{+0.0002}_{-0.0002}$
Kepler-444 e/f	5:4	0.0063	$0.003^{+0.003}_{-0.002}$	$0.002^{+0.003}_{-0.004}$	$0.003^{+0.001}_{-0.002}$	$0.002^{+0.002}_{-0.002}$
Kepler-526 b/02	5:4	0.0064	$0.036^{+0.007}_{-0.013}$	$0.036^{+0.006}_{-0.014}$	$0.008^{+0.006}_{-0.003}$	$0.008^{+0.006}_{-0.003}$
Kepler-549 01/b	5:3	0.0469	$0.015^{+0.006}_{-0.007}$	$0.013^{+0.006}_{-0.009}$	$0.001^{+0.012}_{-0.001}$	$-0.0002^{+0.012}_{-0.001}$
Kepler-1126 b/02	2:1	−0.0807	$0.071^{+0.11}_{-0.055}$	$0.07^{+0.124}_{-0.11}$	$0.062^{+0.011}_{-0.025}$	$0.057^{+0.016}_{-0.02}$

Note. Column (2) lists each planet pair's nearest first- or second-order MMR. Column (3) lists planet pairs' normalized distance to resonance, $\Delta = (j-k)P'/(jP) - 1$, where P and P' are the periods of the inner and outer planet, respectively, and $k = 1$ or 2 as appropriate for a first- or second-order resonance. Values and uncertainties reflect the peak posterior probabilities and 68.3% credible regions, computed as described in the caption of Table 1. Our $\mathcal{Z}$ is defined in terms of *free* eccentricities (Equation (3)), whereas the MCMC outputs total (free+forced) eccentricity; we convert to free eccentricity for this table by subtracting off the analytically calculated forced components.

(This table is available in machine-readable form.)

N-body MCMC, which is not computationally feasible, we complement MCMC simulations with fits using the analytic formulae. The analytic fits convert the amplitudes $\delta\hat{t}_{\mathcal{F}}$, $\delta\hat{t}_{\mathcal{S}}$, and $\delta\hat{t}_{\mathcal{C}}$ measured from TTVs to constraints in the μ'–$|\mathcal{Z}|$ plane. Constraints derived from our analytic fits are compared to the results of the N-body MCMC simulations for each system in the Appendix. The analytic fits lend further confidence to the robustness of MCMC results by showing the degree to which various components of each planet's TTVs constrain planet parameters.

TTVs do not probe planet masses directly, but rather planet–star mass ratios. Therefore, we will often find it convenient to give planet masses in units of

$$M_{\oplus *} \equiv M_{\oplus} \times \left(\frac{M_*}{M_\odot}\right), \tag{7}$$

where $M_*/M_\odot$ is the ratio of host star mass to solar mass. Employing $M_{\oplus *}$ as the unit highlights mass uncertainties inherent to the TTVs separately from those arising from uncertain stellar properties.

Figure 2 compares planet masses inferred using our default versus high-mass priors. Many mass inferences are seen to depend sensitively on the assumed prior, reflecting the degeneracies often inherent to inverting TTV observations.

4. Results

4.1. Masses and Eccentricities

Figure 3 shows inferred TTV planet masses on a mass–radius plot. A sample of transiting planets with RV-measured masses are shown as well for comparison. Most of the planets are less massive than $\lesssim 10\,M_\oplus$ and exhibit a wide diversity of

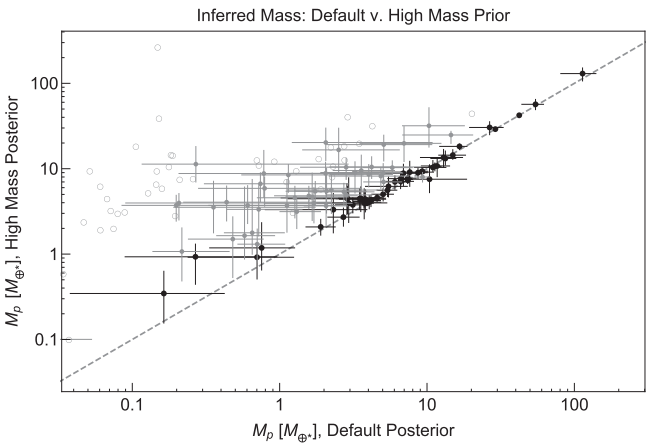

Figure 2. Comparison of planet masses inferred using the high-mass vs. default priors. The dashed line indicates equal mass for both priors. Inferred masses that agree within 1σ (2σ) are shown as black (gray) points. Error bars show 1σ uncertainties. Inferred masses that disagree at $>2\sigma$ are shown as open circles, with error bars omitted for clarity.

radii. Many of the planets are less dense than a hypothetical pure water-composition planet, necessitating the presence of substantial gaseous envelopes to explain their low densities.

Compared to small transiting planets with RV mass measurements, our TTV sample typically finds lower-density planets, as illustrated by Figure 4. Although this trend has been noted before (e.g., Weiss & Marcy 2014; Dai et al. 2015), it is sometimes suggested that this discrepancy is due to mass errors in either the TTV or RV measurements. But Figure 4 demonstrates that much of the discrepancy can be explained if planets farther from the star tend to be less dense—perhaps because they are less affected by photo-evaporation. One should note, however, that the distribution of planets in Figure 4 is also affected by a variety of selection effects. For example, the lack of dense planets at long orbital periods could reflect the decreased transit detectability of small planets with long periods (e.g., Gaidos & Mann 2012). Also, differences between RV and TTV populations could reflect the different dependence of the two techniques on planet mass and radius (e.g., Steffen 2016). Nonetheless, both TTVs and RVs find planets of similar density between periods of 3 days $< P <$ 20 days, where there is significant overlap between the two samples. A simple two-sample Kolmogorov–Smirnov test comparing all densities measured with the two methods gives a probability of $p = 2 \times 10^{-4}$ that they are drawn from the same underlying distribution, while the probability increases to $p = 0.26$ if both samples are restricted to the period range 3 days $< P <$ 20 days.

We turn now to the planets' eccentricities. As discussed in Section 2, although TTV observations do not strongly constrain individual planet eccentricities, they can constrain the combination $\mathcal{Z} \approx (z' - z)/\sqrt{2}$. This combination may be considered as a surrogate for the individual planets' complex eccentricities unless planets have $z \approx z'$, that is, comparable eccentricities and aligned orbits. We expect that planets' complex eccentricities have random relative orientations (see discussion in Paper I) so that, overall, $|\mathcal{Z}|$ values are a reliable surrogate for eccentricities. The inferred values of $|\mathcal{Z}|$ are summarized in Figure 5. The majority of eccentricities are inferred to be small: the median of all the posterior samples shown in Figure 5 is $|\mathcal{Z}| = 0.025$. While many planet pairs' combined eccentricities are small, they are frequently inconsistent with zero.

Table 2 lists combined eccentricities for individual planet pairs. In addition to $|\mathcal{Z}|$, it is of interest to know which planets are consistent with $\mathcal{Z} = 0$; such planets might have experienced significant damping by tides or other effects. Credible regions in $|\mathcal{Z}|$ cannot be used to address this question because $|\mathcal{Z}|$ must be non-negative. Therefore, following Zakamska et al. (2011), we define the signed quantity, $\mathcal{Z}_{\rm proj}$, which is the projection of the $\mathcal{Z}$s from the MCMC posterior onto the median of their distribution. More precisely, we define the median $\mathcal{Z}_{\rm med}$, by computing the median real and imaginary components of $\mathcal{Z}$. Then, given $\mathcal{Z}$, the value of $\mathcal{Z}_{\rm proj}$ is defined as

$$\mathcal{Z}_{\rm proj} = \frac{\mathcal{Z}\mathcal{Z}^*_{\rm med}}{|\mathcal{Z}_{\rm med}|}, \tag{8}$$

where the "*" indicates complex conjugate. Zakamska et al. (2011) show that an analogous quantity is useful for recovering $e = 0$ solutions in the analysis of RV data generated from circular orbits. Of the 90 adjacent planet pairs in our TTV sample, more than 60% have $\mathcal{Z}_{\rm proj}$s inconsistent with 0 at 2σ confidence for both the default and high-mass posteriors.

All planet pairs with at least one robustly measured mass have a robust $\mathcal{Z}_{\rm proj}$ value as well, meaning that the default posterior 1σ credible region in $\mathcal{Z}_{\rm proj}$ contains the high-mass posterior peak likelihood value. There are additional planet pairs with robust $\mathcal{Z}_{\rm proj}$ values in which neither planet has a robust mass value. These pairs tend to have robust $\mathcal{Z}_{\rm proj}$s because the default posterior gives large error bars and not because $\mathcal{Z}_{\rm proj}$ is particularly well constrained by the data. Therefore, we do not label robust and nonrobust $\mathcal{Z}_{\rm proj}$s in Table 2.

4.2. Comparison with Past Work

Here we briefly review how our inferred masses compare with past TTV and RV studies (see the Appendix for discussion of individual systems). Among the 55 planetary systems considered in this work, 24 have appeared in previous TTV or RV analyses. Our results show good agreement with past TTV analyses: the most significant disagreements are between the Mills et al. (2016) derived mass of Kepler-223 c (a 2.4σ disagreement) and the Sanchis-Ojeda et al. (2012) mass of Kepler-30 b (a 1.8σ disagreement). All other robustly inferred planet–star mass ratios are within roughly 1σ of previously reported TTV results.

Some previously reported TTV masses do not meet our requirement for classification as robust. This does not necessarily imply disagreement: for example, Lissauer et al. (2013) report an uncertainty range for Kepler-11 c's mass, which we classify as not robust, that encompasses the range spanned by both the default and high-mass posteriors' 1σ credible regions. In other instances, though, past studies may not have fully explored the sensitivity of their mass measurements to modeling assumptions. For example, Jontof-Hutter et al. (2014) report a mass for Kepler-79 c that agrees well with the default posterior value but disagrees with the high-mass posterior value at $\sim 2.5\sigma$ significance.

A handful of planets in our systems also have RV observations: Kepler-9, Kepler-18, Kepler-25, Kepler-48, Kepler-56, and Kepler-89. Agreement between our TTV constraints and RV mass determinations is mixed, giving consistent results in roughly half of cases and inconsistent

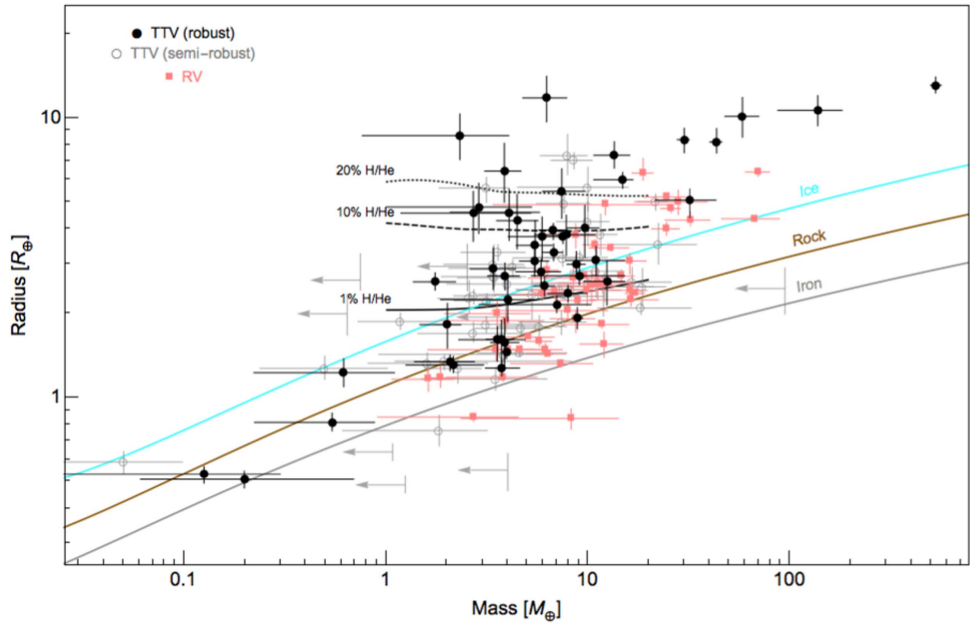

Figure 3. Planet radius vs. mass. Masses from TTVs fit in the Appendix for planets classified as robust as defined in Section 3 are plotted as black circles. Also shown as gray circles are planets whose masses under the two posteriors differ by up to 2σ ("semi-robust"). Error bars indicate the 1σ credible regions from the default posteriors. Planets with RV mass measurements, listed in Table 3, are shown as pink squares. For planets with masses that are consistent with zero, 1σ upper bounds from the high-mass posterior are indicated with an arrow. Planet masses have been converted to units of $M_\oplus$ by multiplying stellar mass and planet–star mass ratios and accounting for stellar mass uncertainties (see Table 1 note for details). Theoretical mass–radius relationships for pure ice, rock, and iron compositions from Fortney et al. (2007) are plotted as colored curves. Mass–radius relationships for planets with Earth-composition cores and H/He envelopes that make up 1%, 10%, and 20% of the total planet mass are plotted as black curves, which are interpolated from Tables 2 and 3 of Lopez & Fortney (2014) assuming an age of 5 Gyr and an incident stellar flux 100 times greater than that of Earth.

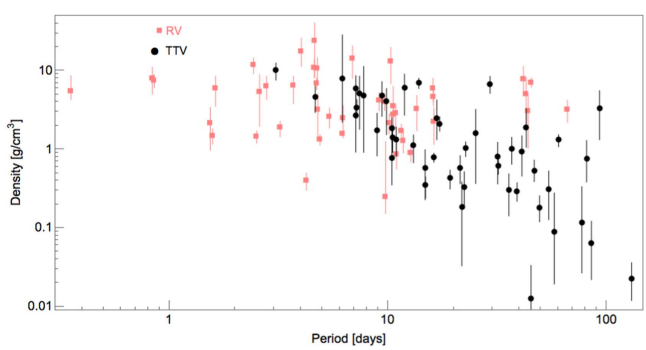

Figure 4. Planet densities vs. orbital period for planets with masses measured via TTV (black circles) and RV (pink squares). TTV planet densities are from the "robust" sample, with default posteriors.

constraints in the other half. It is unclear whether the TTV or RV mass measurements are incorrect (see Appendix).

Libration in MMR is rare among multiplanet *Kepler* systems (Lissauer et al. 2011b; Fabrycky et al. 2014), and this is generally true of our TTV sample as well. A handful of systems in our TTV sample are strongly affected by resonances: Kepler-29, Kepler-60, Kepler-80, and Kepler-223. Dynamical analyses of each of these systems have appeared elsewhere in the literature, and we find similar conclusions to these past works.

5. Discussion

5.1. Gaseous Envelopes

Many of the planets shown in Figure 3 have such low densities that they must have massive gaseous envelopes. Such massive envelopes were likely accreted when the protoplanetary disk was

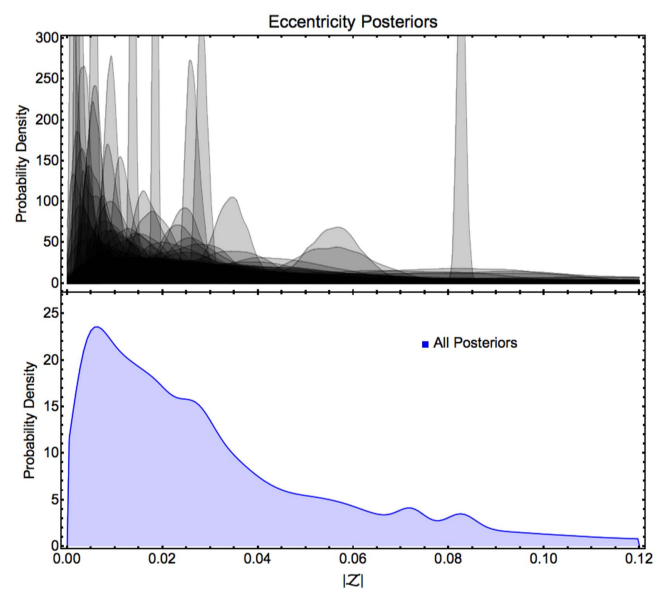

Figure 5. Top panel: posterior probability distributions of combined eccentricities, $|\mathcal{Z}|$, for all adjacent planet pairs (both robust and otherwise) from N-body MCMC fits. The probability distributions are computed by applying a Gaussian kernel density estimate to the N-body MCMC default posterior samples. Kernel bandwidths, h, are chosen using the "Silverman rule," $h = 1.06\sigma N^{-1/5}$, where σ is the sample variance and N is the number of samples (Silverman 1986). Combined eccentricities are shown only for adjacent planet pairs; combined eccentricities of nonadjacent planets are typically poorly constrained. Bottom panel: smoothed histogram computed by combining all posterior samples shown in the top panel, using a bandwidth $h = 0.003$. The resulting "distribution" illustrates the typical magnitudes of combined eccentricities shown in the top panel, though it does not represent a true probability distribution.

Table 3
Transiting RV Planets

Name	Period (days)	Mass ($M_\oplus$)	Radius ($R_\oplus$)	Reference
Kepler-4 b	3.21	$24.5^{+3.8}_{-3.8}$	$4.0^{+0.2}_{-0.2}$	Borucki et al. (2010)
CoRoT-7 b	0.85	$5.7^{+0.9}_{-0.9}$	$1.6^{+0.1}_{-0.1}$	Barros et al. (2014)
CoRoT-8 b	6.21	$69.9^{+9.5}_{-9.5}$	$6.4^{+0.2}_{-0.2}$	Bordé et al. (2010)
Kepler-10 b	0.84	$4.6^{+1.3}_{-1.5}$	$1.5^{+0.05}_{-0.03}$	Esteves et al. (2015)
Kepler-10 c	45.29	$17.2^{+1.9}_{-1.9}$	$2.4^{+0.1}_{-0.04}$	Dumusque et al. (2014)
HAT-P-11 b	4.89	$25.7^{+2.9}_{-2.9}$	$4.7^{+0.2}_{-0.2}$	Bakos et al. (2010)
Kepler-20 b	3.70	$8.7^{+2.1}_{-2.2}$	$1.9^{+0.1}_{-0.2}$	Gautier et al. (2012)
Kepler-20 c	10.85	$16.1^{+3.3}_{-3.7}$	$3.1^{+0.2}_{-0.3}$	Gautier et al. (2012)
CoRoT-22 b	9.76	$12.2^{+14.}_{-8.8}$	$4.9^{+0.2}_{-0.4}$	Moutou et al. (2014)
CoRoT-24 c	11.76	$28.0^{+11.}_{-11.}$	$5.0^{+0.5}_{-0.5}$	Alonso et al. (2014)
HAT-P-26 b	4.23	$18.8^{+2.2}_{-2.2}$	$6.3^{+0.8}_{-0.4}$	Hartman et al. (2011)
Kepler-48 d	42.90	$7.9^{+4.6}_{-4.6}$	$2.0^{+0.1}_{-0.1}$	Marcy et al. (2014)
Kepler-68 b	5.40	$8.3^{+2.2}_{-2.4}$	$2.3^{+0.1}_{-0.1}$	Gilliland et al. (2013)
Kepler-68 c	9.61	$4.8^{+2.5}_{-3.6}$	$1.0^{+0.04}_{-0.04}$	Gilliland et al. (2013)
Kepler-78 b	0.36	$1.9^{+0.4}_{-0.2}$	$1.2^{+0.2}_{-0.1}$	Pepe et al. (2013)
Kepler-93 b	4.73	$4.0^{+0.7}_{-0.7}$	$1.5^{+0.02}_{-0.02}$	Dressing et al. (2015)
Kepler-94 b	2.51	$10.8^{+1.4}_{-1.4}$	$3.5^{+0.1}_{-0.1}$	Marcy et al. (2014)
Kepler-95 b	11.52	$13.0^{+2.9}_{-2.9}$	$3.4^{+0.1}_{-0.1}$	Marcy et al. (2014)
Kepler-96 b	16.24	$8.5^{+3.4}_{-3.4}$	$2.7^{+0.2}_{-0.2}$	Marcy et al. (2014)
Kepler-97 b	2.59	$3.5^{+1.9}_{-1.9}$	$1.5^{+0.1}_{-0.1}$	Marcy et al. (2014)
Kepler-98 b	1.54	$3.5^{+1.6}_{-1.6}$	$2.0^{+0.2}_{-0.2}$	Marcy et al. (2014)
Kepler-99 b	4.60	$6.2^{+1.3}_{-1.3}$	$1.5^{+0.1}_{-0.1}$	Marcy et al. (2014)
Kepler-100 b	6.89	$7.3^{+3.2}_{-3.2}$	$1.3^{+0.04}_{-0.04}$	Marcy et al. (2014)
Kepler-102 d	10.31	$3.8^{+1.8}_{-1.8}$	$1.2^{+0.04}_{-0.04}$	Marcy et al. (2014)
Kepler-102 e	16.15	$8.9^{+2.}_{-2.}$	$2.2^{+0.1}_{-0.1}$	Marcy et al. (2014)
Kepler-106 c	13.57	$10.4^{+3.2}_{-3.2}$	$2.5^{+0.3}_{-0.3}$	Marcy et al. (2014)
Kepler-106 e	43.84	$11.2^{+5.8}_{-5.8}$	$2.6^{+0.3}_{-0.3}$	Marcy et al. (2014)
Kepler-113 b	4.75	$11.7^{+4.2}_{-4.2}$	$1.8^{+0.05}_{-0.05}$	Marcy et al. (2014)
Kepler-131 b	16.09	$16.1^{+3.5}_{-3.5}$	$2.4^{+0.2}_{-0.2}$	Marcy et al. (2014)
Kepler-131 c	25.52	$8.2^{+5.9}_{-5.9}$	$0.8^{+0.1}_{-0.1}$	Marcy et al. (2014)
KOI-142 b	10.95	$8.7^{+2.5}_{-2.5}$	$3.8^{+0.4}_{-0.4}$	Nesvorný et al. (2013)
Kepler-406 b	2.43	$6.3^{+1.4}_{-1.4}$	$1.4^{+0.03}_{-0.03}$	Marcy et al. (2014)
Kepler-406 c	4.62	$2.7^{+1.8}_{-1.8}$	$0.8^{+0.03}_{-0.03}$	Marcy et al. (2014)
Kepler-413 b	66.26	$67.0^{+22.}_{-21.}$	$4.3^{+0.1}_{-0.1}$	Kostov et al. (2014)
Kepler-454 b	10.57	$6.8^{+1.4}_{-1.4}$	$2.4^{+0.1}_{-0.1}$	Gettel et al. (2016)
GJ 1132 b	1.63	$1.6^{+0.6}_{-0.6}$	$1.2^{+0.1}_{-0.1}$	Berta-Thompson et al. (2015)
GJ 1214 b	1.58	$6.3^{+0.9}_{-0.9}$	$2.8^{+0.2}_{-0.2}$	Harpsøe et al. (2013)
HIP 116454 b	9.12	$11.8^{+1.3}_{-1.3}$	$2.5^{+0.2}_{-0.2}$	Vanderburg et al. (2015)
K2-38 b	4.02	$12.0^{+2.9}_{-2.9}$	$1.6^{+0.2}_{-0.2}$	Sinukoff et al. (2016)
K2-38 c	10.56	$9.9^{+4.6}_{-4.6}$	$2.4^{+0.3}_{-0.3}$	Sinukoff et al. (2016)
BD+20 594 b	41.69	$16.3^{+6.}_{-6.1}$	$2.2^{+0.1}_{-0.1}$	Espinoza et al. (2016)

Note. Periods, masses, and radii of transiting RV planets smaller than 8 $R_\oplus$. All planets have been selected from the exoplanet archive. Only planets with 1σ mass uncertainties inconsistent with 0 are included. We exclude RV measurements of planets from the Kepler-18, 25, 48, and 89 systems since they are also in our TTV sample.

(This table is available in machine-readable form.)

still present; outgassing can only produce envelopes less massive than ~2% of a planet's total mass (Rogers et al. 2011). Here we convert observed masses and radii to envelope masses by interpolating the tables of Lopez & Fortney (2014). Those authors simulate envelopes on top of Earth-composition cores; as time proceeds, their envelopes cool, while being irradiated by the star. Thus, the masses and radii of their envelopes are essentially related by the fact that the cooling time should be comparable to the age. Although there are multiple unknowns that will affect the predicted envelope mass (especially atmospheric opacity and composition and, to a lesser extent, the core composition and heating/cooling; see, e.g., Rogers et al. 2011; Howe et al. 2014; Lopez & Fortney 2014), the results of their simulations are adequate for our purposes.

Inferred envelope mass fractions, $M_{\rm env}/M_p$, are plotted in Figure 6 for planets more massive than 1 $M_\oplus$ and smaller than 8 $R_\oplus$ with either RV or robust TTV mass measurements. Lopez & Fortney (2014) find that the radii of planets with envelope mass fractions $\gtrsim$1% are quite insensitive to core mass. Therefore, the diversity of gas fractions in Figure 6 reflects the diversity of radii seen in Figure 3. On the other hand, inferred envelope mass fractions $\lesssim$1% are likely sensitive to our assumption of Earth-composition cores, and some of the envelope mass fractions in Figure 6 may actually reflect a diversity of core compositions.

How do the inferred envelopes shown in Figure 6 compare to theoretical predictions of gas envelope accretion? A number of studies have examined envelope accretion by planetary cores embedded in a gaseous protoplanetary disk (e.g., Ikoma & Hori 2012; Bodenheimer & Lissauer 2014; Ginzburg et al. 2016; Lee & Chiang 2016). These studies find that super-Earth cores readily accrete envelopes between a few to tens of percent of their total mass over the lifetime of a protoplanetary disk, similar to those shown in Figure 6. Planets in Figure 6 that are consistent with having no envelope generally receive higher fluxes than similar-mass planets covered by significant envelopes. This trend could result from photoevaporation removing the envelopes initially accreted by planets close to their stars (e.g., Lopez et al. 2012; Owen & Wu 2013). Especially low-mass, low-density "super-puff" planets are of particular interest from a formation standpoint. We identify five planets with robust mass measurements and gas fractions above 10% at $>1\sigma$ confidence: Kepler-18 d (29% ± 4%), Kepler-51 c (35^{+20}_{-14}%), Kepler-177 c (50% ± 10%), Kepler-279 b (23^{+10}_{-9}%), and Kepler-359 c (18^{+8}_{-7}%). Explaining how such planets manage to accrete and retain such large gaseous envelopes while avoiding runaway gas accretion presents an interesting theoretical challenge (e.g., Lee & Chiang 2016). Among planets that do have significant envelopes, there is no obvious trend in envelope fraction with planet mass. This suggests a wide diversity of factors that influence envelope accretion and retention.

5.2. Eccentricities

Overall, our results show that most planets have relatively small eccentricities of a few percent. This is consistent with the results of past TTV studies (Wu & Lithwick 2013; Hadden & Lithwick 2014) and transit duration analyses (Van Eylen & Albrecht 2015; Xie et al. 2016) of multiplanet systems. These studies infer the overall eccentricity distribution of their samples by fitting Rayleigh distributions: Wu & Lithwick (2013) find a mean eccentricity $\bar{e} \sim 0.01$ for a sample of 44 planets, Hadden & Lithwick (2014) find $0.02 < \bar{e} < 0.03$ for a sample of 139 planets, Van Eylen & Albrecht (2015) find $0.05 < \bar{e} < 0.08$ for a sample of 74 planets, and Xie et al. (2016) find $\bar{e} < 0.07$ for a sample of 330 planets. In contrast to these population-level studies, we are able to measure the combined eccentricities of individual planet pairs, often with uncertainties on the order of a percent or better. Both Van Eylen & Albrecht (2015) and Xie et al. (2016) suggest that

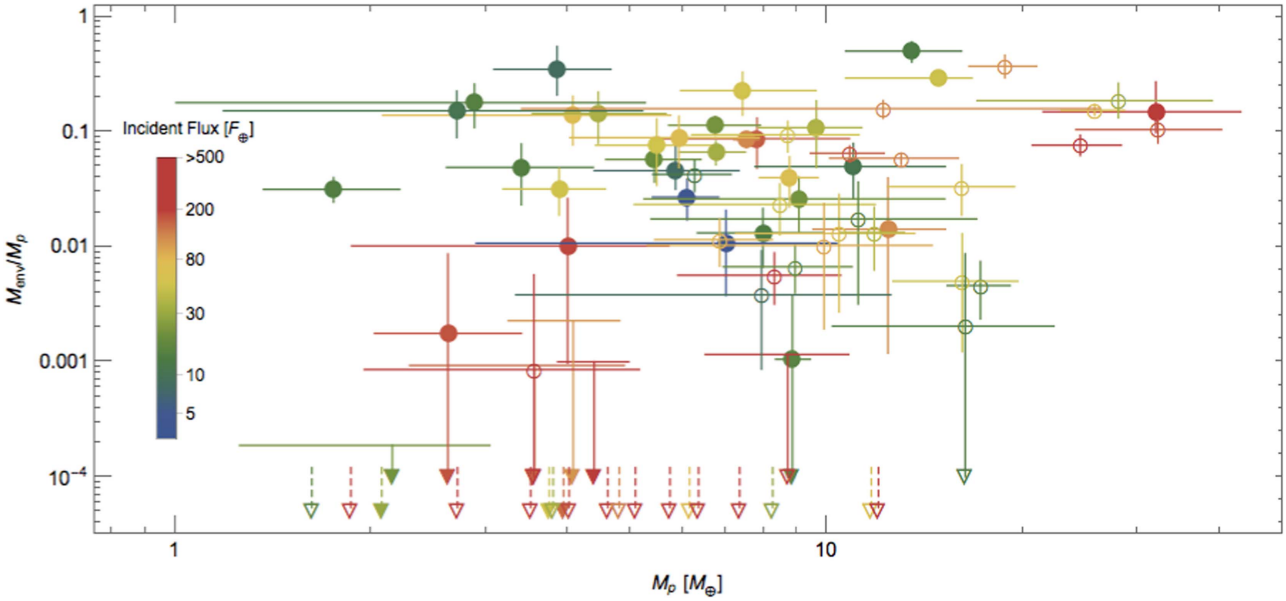

Figure 6. Envelope mass fraction vs. planet mass. TTV planets and RV planets are shown with filled and open symbols, respectively. Planets' incident fluxes are indicated by color scale. Envelope mass fractions are computed assuming an age of 5 Gyr from Tables 2 and 3 in Lopez & Fortney (2014) via interpolation. Error bars show 1σ uncertainties. Error bars extending below $M_{\rm env}/M_p < 10^{-4}$ are indicated with arrows. Points with error bars entirely below $M_{\rm env}/M_p < 10^{-4}$ are indicated with dashed arrows, and mass error bars are omitted for clarity.

TTV systems' proximity to resonance may imply eccentricities that are distinct from the larger population of multiplanet systems. While it is true that TTV systems are preferentially closer to resonance, they are not as radically distinct from the larger multiplanet population in their proximity to resonance as is often suggested (see Figure 8 in the Appendix).

As noted above, a majority of the objects in our TTV sample (roughly 60%) have eccentricities that are nonzero at 2σ confidence. This seemingly contradicts the inference that the planets were born in a disk of gas, which would presumably damp eccentricities. The nonzero eccentricities suggest that planets may have accreted their envelopes from a depleted disk in which gas damping was ineffective (Lee & Chiang 2016).

Some of the planets in Table 1 orbit their host star at close enough separations that their eccentricities may be affected by tidal dissipation. Tidal dissipation depends steeply on planet period, and the shortest-period planets are expected to have experienced significant tidal damping. Figure 7 plots $\mathcal{Z}_{\rm proj}$ (Equation (8)) versus the periods of planet pairs' inner planets. All but one of the seven shortest-period planets within $P \lesssim 5$ days have combined eccentricities consistent with 0, suggesting circularization by tides. The shortest-period planet, Kepler-80 d, has a small but nonzero $\mathcal{Z}_{\rm proj}$. Beyond periods of 5 days there is a mixture of combined eccentricities that are consistent with 0 or very nearly so, as well as combined eccentricities that are definitively nonzero.

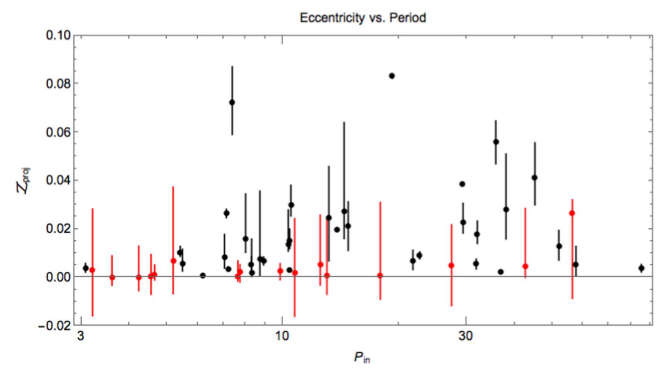

Figure 7. Signed combined eccentricities, $\mathcal{Z}_{\rm proj}$ (Equation (8)), vs. period for adjacent planet pairs. Error bars indicate 1σ credible regions computed with the default prior. $\mathcal{Z}_{\rm proj}$ values that are consistent with 0 at the 1σ level are emphasized as red points. Only combined eccentricities that are robustly measured, meaning that the default posterior 1σ credible region contains the high-mass posterior peak likelihood value, are plotted. We have also excluded points with 1σ credible regions larger than 0.05 for clarity.

6. Summary and Conclusion

We have presented a uniform analysis of the TTVs of 55 multiplanet systems in order to infer planet masses and eccentricities. We employ both N-body and analytic fitting in a complementary approach in order to identify the degeneracies inherent to TTV inversion and understand when and how they are broken by components of the TTV signal. We use two sets of MCMC simulations for each system, each of which uses a prior weighted to opposite extremes of the mass–eccentricity degeneracy predicted by the analytic formulae, in order to classify inferred planet masses as robust or not.

Low-mass ($\lesssim 10 M_\oplus$) planets exhibit a wide diversity of sizes, with many of these planets less dense than a hypothetical pure ice composition planet, indicating the presence of significant gaseous envelopes. The wide diversity of planet sizes can be attributed to a diversity of planet envelope mass fractions. We use our TTV fits, together with the evolutionary models of Lopez & Fortney (2014), to convert planet masses and radii to envelope mass fractions. We plan to use our sample of TTV-characterized planets in a future work examining planets' accretion and retention of gas envelopes during and after dispersal of the protoplanetary disk.

With guidance from the analytic TTV model, we have focused on planets' combined eccentricities, $\mathcal{Z}$, rather than individual eccentricities, which are largely unconstrained by TTVs. We find that planets typically have eccentricities of a

few percent or less, in agreement with past statistical studies of multiplanet systems (Wu & Lithwick 2013; Hadden & Lithwick 2014; Van Eylen & Albrecht 2015; Xie et al. 2016). The shortest-period planets have eccentricities consistent with 0 and thus may have experienced significant tidal eccentricity damping. Detailed modeling of individual TTV systems can potentially shed light on how dynamical processes such as migration and eccentricity damping may have shaped the systems we observe today.

We measure a number of planet masses for planets in the super-Earth/mini-Neptune size range where there is great theoretical interest in understanding the mass–radius relationship. The observational biases of our TTV sample are difficult to assess given the TTV signal's complicated dependence on periods and eccentricities. We see incorporating TTV non-detections and quantifying selection effects as important directions for future work in understanding the mass–radius relationship.

We thank Lauren Weiss for helpful discussion and the anonymous referee for helpful comments. We are grateful to the Kepler team for acquiring and publicly releasing such spectacular results. This research has made use of the NASA Exoplanet Archive, which is operated by the California Institute of Technology, under contract with the National Aeronautics and Space Administration under the Exoplanet Exploration Program. S.H. acknowledges support from the NASA Earth and Space Science Fellowship program, grant no. NNX15AT51H. Y.L. acknowledges grants AST-1109776 and AST-1352369 from NSF and NNX14AD21G from NASA.

Appendix
Description of Individual Systems

Our initial selection of systems is made from TTVs identified in the Q1–17 catalog of Holczer et al. (2016). We limit our selection to multiplanet systems hosting at least one planet pair with a period ratio smaller than $P'/P < 2.2$. After selecting systems on the basis of period ratios, we identify planets with significant TTVs as follows.

1. Each planet's transit times are fit with two linear models: the first is a simple linear trend corresponding to a constant orbital period, and the second fits each planet's transit times as a linear trend plus a TTV induced by the other planets in the system. The TTV is assumed to be described by Equation (1) and parameterized by the amplitudes $\hat{\delta t_{\mathcal{F}}}$, $\hat{\delta t_{\mathcal{S}}}$, and $\hat{\delta t_{\mathcal{C}}}$. Since $P_{\rm sup}$ and $P_{\rm syn}$ in Equation (1) are defined in terms of "average" orbital periods that differ from the orbital period fit without accounting for TTVs, fits are iterated to achieve convergence in average orbital periods.
2. We compute the Bayesian Information Criterion (BIC; Schwarz 1978), defined as

$$\mathrm{BIC} = \chi^2 + k \ln(N_{\rm trans.}) \tag{9}$$

for both linear fits of a planet's transit times, where χ^2 has the standard definition, k is the number of fit parameters, and $N_{\rm trans.}$ is the number of transit times that are fit. We select TTVs for which the sinusoidal fit improves the BIC by >10 relative to the simple linear trend model, indicating very strong evidence for the analytic TTV model over the simple linear trend (Kass & Raftery 2012).
3. Finally, we remove a handful of systems after visual inspection of the analytic fit (KOI-0295, KOI-0571, KOI-1873, KOI-2029) or because we are unable to find a satisfactory initial N-body fit (KOI-262, KOI-880, KOI-1426, KOI-2693), potentially because of nontransiting perturbers.

In systems with three or more planets, any planets that are separated from the next adjacent planet by a period ratio greater than $P'/P > 2.2$ are ignored by our analysis.[6] Figure 8 compares our selected sample to all confirmed *Kepler* planet pairs with $P'/P < 2.2$, showing both period ratios and normalized distance to the nearest first- or second-order MMR,

$$\Delta = \frac{j-k}{j}\frac{P'}{P} - 1, \tag{10}$$

with $k = 1, 2$ or as appropriate for first- or second-order MMRs. The TTV sample is biased toward closer period ratios compared to the complete multiplanet sample, largely because it lacks planets between the 3:2 and 2:1 MMRs. It is often claimed that because TTV systems contain planets close to MMRs they may have unique formation channels not shared with the broader population of multiplanet systems. The proximity to resonance of our sample, as measured by Δ, is compared to the full sample of multiplanet systems in Figure 8. Pairs with $|\Delta| > 0.05$, which constitute $\sim$30% of the total sample, are essentially absent from the TTV sample. Otherwise, the TTV sample is not radically distinct in its proximity to resonance.

Our MCMC fits the transit times computed by Rowe et al. (2015) from long-cadence *Kepler* data. We assume Gaussian transit time uncertainties and remove $>4\sigma$ outliers after an initial least-squares fit, as described in Paper I. At least one observing quarter of short-cadence data is available for every system in our TTV sample except Kepler-1126. In future work, short-cadence data could yield improved constraints on planet properties. However, it is unclear how much improvement short-cadence data offer: Jontof-Hutter et al. (2016) fit transit times computed with all available short-cadence data for eight systems in our TTV sample, and they measure masses with roughly the same precision as those reported here.

The MCMC results do not include dynamical stability considerations, which can rule out planet parameters that produce rapid dynamical instability. We investigate dynamical stability by running 500 N-body integrations of each system with initial conditions drawn randomly from the MCMC posterior distributions. Each integration is run for 10^6 orbits of the innermost planet using the REBOUND code's WHFast integrator (Rein & Tamayo 2015). Five of the 55 TTV systems are unstable in more than 10% of the integrations initialized from the default posteriors: Kepler-24, Kepler-60, Kepler-122, Kepler-223, and Kepler-1126. With the exception of Kepler-60, stability considerations do not have a significant influence on inferred planet parameters in these systems (see discussions of individual systems below), so we do not attempt to adjust our reported masses and combined eccentricities for these

[6] Two exceptions to this cut, Kepler-52 d and Kepler-27.03, were included in our fits before we arrived at our final selection criteria. These planets are included in our posterior data, though neither contributes useful constraints.

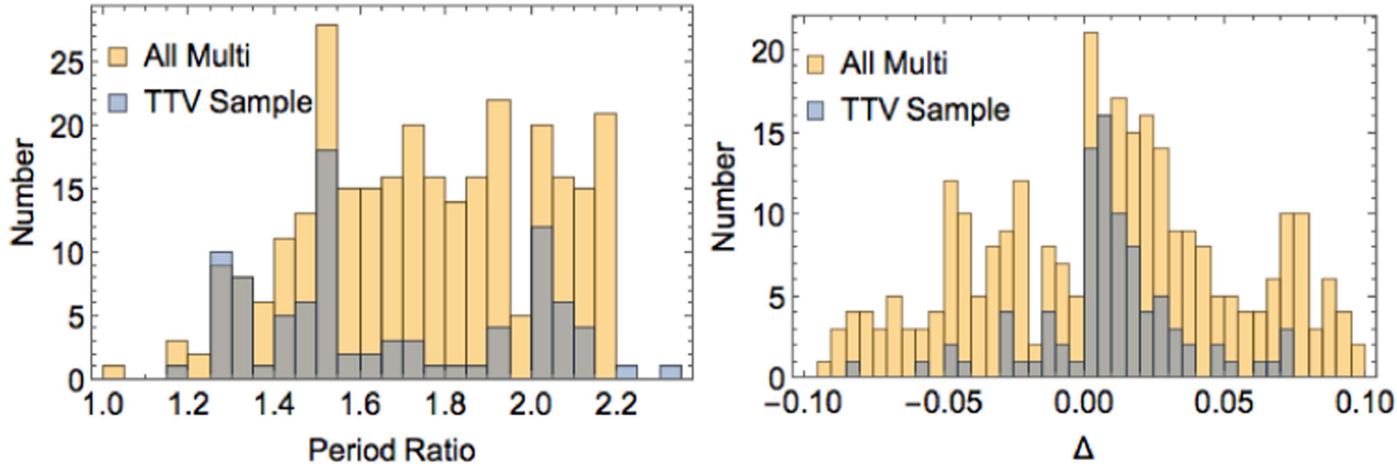

Figure 8. Comparison of our selected TTV sample to all *Kepler* multiple-transiting planets. The "All Multi" sample contains all confirmed pairs of planets with period ratios less than $P'/P < 2.2$ taken from the Exoplanet Archive on 2016 November 4. Left panel: histogram of the period ratios of adjacent planet pairs. Right panel: histogram of distances to the nearest first- or second-order resonance, Δ, defined in Equation (10).

systems. Integrations initialized from the high-mass posteriors never produce instability in more than a few instances with the exception of Kepler-223, for which 38/500 integrations are unstable.

The posterior samples from our MCMC fits, along with plots showing the TTVs of each system, are available online (10.5281/zenodo.162965). Each system is discussed below (see Paper I for discussion of the Kepler-26, Kepler-33, Kepler-128, and Kepler-307 systems). Systems have been categorized into four groups based on the analytic fits.

1. *Chopping systems* are presented in Appendix A.1. These systems host at least one planet with a chopping signal that allows the mass–eccentricity degeneracy to be broken, resulting in constraints on planet masses and combined eccentricities. The chopping signal constrains the mass of a perturbing companion. With the perturber's mass constrained, the TTV signal component caused by a first- or second-order MMR uniquely determines the planets' combined eccentricity. Some systems where a lack of chopping places a strong upper bound on planet masses are also included in this category.
2. *Second-harmonic systems* are presented in Appendix A.2. This group is composed of systems with a pair of planets near a first-order MMR. The second-harmonic TTV of at least one of the planets helps break the mass–eccentricity degeneracy. The second-harmonic TTV often does not provide as strong a constraint on planet mass as the chopping TTV. In most cases, the second-harmonic TTV sets an upper limit to the combined eccentricity, or equivalently, a lower limit on planet masses.
3. *Resonant and massive systems* include systems that have planets either extremely close to or librating in resonance or systems with especially massive planets. The analytic formulae are not expected to provide accurate approximations of the TTVs of such planets.
4. *Degenerate systems* do not have significant chopping or second-harmonic signals and show a strong degeneracy between masses or eccentricities. These systems are summarized in Appendix A.4.

Below, analytic fits are compared to *N*-body results in a series of "analytic constraint plots." To generate these plots, we convert the 1σ uncertainties in $\delta\hat{t}_{\mathcal{F}}$, $\delta\hat{t}_{\mathcal{S}}$, and $\delta\hat{t}_{\mathcal{C}}$ obtained from least-squares fitting to 1σ uncertainty bands in the μ'-$|\mathcal{Z}|$ plane.[7] The details of this procedure are described in Paper I. Planets with robustly inferred masses, as defined in Section 3, are indicated with an asterisk.

A.1. Chopping Systems

Kepler-11 b, c, d, e*, f** (Figure 9): The inner five planets of Kepler-11 are near a series of first- and second-order MMRs. The TTVs robustly constrain the masses of planets d, e, and f. The bottom left panel of Figure 9 shows that the masses of planets d and e are strongly constrained by their mutual chopping TTVs. The bottom right panel of Figure 9 summarizes the constraints from the interaction of planets e and f. Since the mass of planet e is already constrained by its interaction with planet d, planet f's fundamental TTV constrains the e/f pair's combined eccentricity. The combination of planet e's fundamental and chopping TTV constrains the mass of planet f.

The masses of the innermost pair, b and c, are less robust to the choice of priors. The top left panel of Figure 9 shows that their inferred properties are consistent with their fundamental TTVs and that their lack of chopping TTVs imposes upper bounds on their masses.

The upper right panel of Figure 9 shows that planet c's chopping TTV gives a weak constraint on planet d's mass, and the lack of chopping in planet d's TTV gives an upper limit to the mass of planet c. Planets c and d are not close to any first or second-order MMRs, so there is little correlation between their masses and combined eccentricity.

[7] Chopping amplitude constraints are computed by incorporating the prior assumption that masses are non-negative. This constraint affects the 1σ upper limits computed for $\delta\hat{t}_{\mathcal{C}}$ values that are consistent with negative masses. The analytic model is formulated in terms of *free* eccentricities, whereas the MCMC outputs total (free+forced) eccentricity. While the distinction is usually negligible, there are some instances below where planets' forced and free eccentricities are of comparable magnitude. In these instances, we correct the *N*-body MCMC results shown in the constraint plots by subtracting off forced eccentricity components. The forced components are computed analytically as the eccentricities induced by the nearest three first-order MMRs (see, e.g., Equation (13) of Lithwick et al. 2012); other nonresonant contributions to the forced eccentricity are negligible. We note explicitly in figure captions when such a correction has been applied.

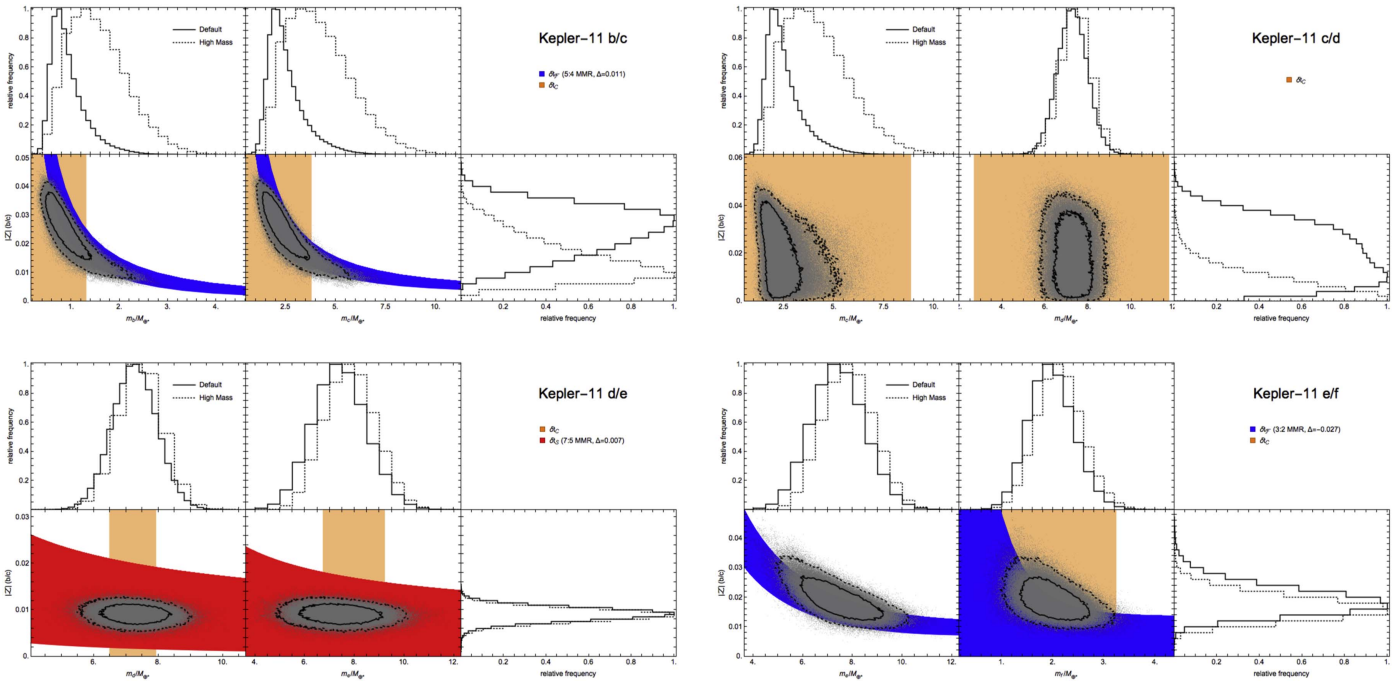

Figure 9. Constraint plots for the Kepler-11 system. Each panel summarizes the constraints derived from the interactions of a particular planet pair. Specifically, the constraints placed *by* the TTV of the outer planet *on* the mass of the inner planet plus the combined eccentricity are shown in the bottom left panel, and the constraints of the inner planet's TTV on the outer planet's properties are shown in the bottom middle panel. Posterior samples from the default prior MCMC are plotted as gray points, with black lines indicating the 68% (solid) and 95% (dashed) credible regions. Histograms show the marginalized mass and combined eccentricity posterior distributions from the default prior (solid) and high-mass prior (dotted) *N*-body MCMCs. The 1σ constraints from fundamental TTVs are shown in blue, chopping TTVs in orange, and second-harmonic/second-order resonance TTVs in red. Note that planet masses are plotted relative to the host star mass in units of $M_{\oplus *}$ defined in Equation (7).

(The complete figure set (83 images) is available.)

TTV analyses of the Kepler-11 system have been conducted by number of authors (Lissauer et al. 2011a; Migaszewski et al. 2012; Lissauer et al. 2013; Borsato et al. 2014), and our results agree well with previous work. We omit the outermost planet of the system, Kepler-11 g, from our analysis since it does significantly influence the TTVs of the other planets (Lissauer et al. 2011a).

Kepler-18 c, d* Figure 9.5): Planet d's inferred mass agrees well with the analytic chopping constraint. The chopping amplitude measurement has a fractional uncertainty of ∼50%, so there is still a large degree of mass–eccentricity degeneracy. Consequently, planet c's mass does not meet our standard for classification as robust.

Kepler-18 was previously analyzed by Cochran et al. (2011), who fit both RV and TTV observations of Kepler-18 spanning Quarters 0–6. They find planet masses of $[m_c, m_d] = [17.3 \pm 1.9, 16.4 \pm 1.4]\ M_\oplus$ using a combination of RV and TTV data. Their results are consistent with our *N*-body MCMC fits.

Kepler-18 hosts an additional planet, b, interior to planet c. The TTVs of planet b appear flat, and we find that including it in our *N*-body MCMC fitting does not yield a strong constraint on its properties or affect the inferred properties of planets c and d.

Kepler-49 b**,c** (Figure 9.6): Planet b's chopping TTV breaks the mass–eccentricity degeneracy for this planet pair, resulting in two robustly inferred masses. Jontof-Hutter et al. (2016) fit masses $[m_b, m_c] = [9.2^{+3.7}_{-3.5}, 5.9^{+2.7}_{-2.3}]\ M_\oplus$ analyzing Q1–17 transit times of Kepler-49 b and c, in good agreement with the default prior MCMC results, $[m_b, m_c] = [8.1^{+1.8}_{-1.8}, 5.8^{+1.5}_{-1.4}]\ M_\oplus$.

Kepler-51 b**, c***, d** (Figures 9.7–9.8): The masses of planets c and d are well constrained by their mutual chopping TTVs. The combined eccentricity of planets b and c is constrained by the fundamental TTV of planet b since the mass of planet c is already constrained by its effect on planet d. Masuda (2014) previously conducted an MCMC analysis of the Kepler-51 system's TTVs using *Kepler* data spanning Quarters 1–16 and fit masses $[m_b, m_c, m_d] = [2.1^{+1.5}_{-0.8}, 4.0 \pm 0.4, 7.6 \pm 1.1]\ M_\oplus$. The masses found by Masuda (2014) agree well with our default prior results: $[m_b, m_c, m_d] = [2.4^{+1.7}_{-1.6}, 3.8^{+0.9}_{-0.7}, 6.2^{+1.6}_{-1.5}]\ M_\oplus$.

Kepler-58 b, c (Figure 9.9): Kepler-58 b's and c's lack of chopping place upper bounds on the planets' masses that agree well with the upper limits inferred from the high-mass prior *N*-body MCMC results.

Kepler-79 b, c, d, e* (Figures 9.10–9.12): The planets of the Kepler-79 system are near a succession of first-order MMRs: 2:1 (b/c), 2:1 (c/d), and 3:2 (d/e). Planet e's mass is robustly constrained and shows fair agreement with the analytic chopping constraint. Jontof-Hutter et al. (2014) also analyze the TTVs of the Kepler-79 system using Q1–14 short-cadence data. Their results agree with ours for the robustly measured mass of planet e.

Kepler-84 d, b, c, e, f (Figures 9.13–9.16): Kepler-84 hosts five planets near a series of first- and second-order MMRs. Planet f's chopping TTV favors a planet e mass of $m_e \sim 40\ M_{\oplus *}$, though the default prior's weighting toward low masses results in a posterior that is consistent with $m_e = 0$. The other planets suffer strong mass–eccentricity degeneracies or have weak mass upper bounds from the nondetection of TTVs.

Kepler-85 b, c, d, e* (Figures 9.17–9.20): Kepler-85 c's, d's, and e's lack of strong chopping TTVs places upper bounds on planet c's and d's masses. Planets b and c have significant

fundamental TTVs from their near 3:2 commensurability. Planet b's and c's TTVs are subject to the mass–eccentricity degeneracy. Planet e's mass is robust based on the MCMC results, though it is not clear from the analytic constraints shown in Figures 9.19 and 9.20 why this is the case. An analytic MCMC fit to Kepler-85's TTVs yields $m_e = 2.8^{+1.6}_{-2.0}\, M_{\oplus *}$, consistent with, though more uncertain than, the *N*-body MCMC results. We are unable to fully account for Kepler-85 e's well-constrained mass with the analytic model.

Kepler-105 03, b, c* (Figures 9.21–9.22): Planet c's mass is robustly constrained by chopping. KOI-115.03 and Kepler-105 b do not induce significant variations in each other's transit times, imposing an upper limit that agrees well with the high-mass prior *N*-body results. Jontof-Hutter et al. (2016) measure planet c's mass to be $m_c = 4.6 \pm 0.9\, M_{\oplus *}$ from an analysis of Q1–17 transit times, consistent with our inferred value, $m_c = 2.9 \pm 1.5\, M_{\oplus *}$ at roughly 1σ confidence.

Kepler-127 b, c, d (Figures 9.23–9.24): Figure 9.24 shows that planet d's mass is constrained by chopping. Consequently, the combined eccentricity of c and d is well constrained by their 5:3 MMR TTVs. Planet c's mass is inferred to be slightly lower than the chopping constraint, though its inferred mass is not robust to the choice of priors. The 2:1 fundamental TTVs of planets b and c suffer a strong mass–eccentricity degeneracy.

Kepler-138 b, c, d (Figures 9.25–9.26): Planet d's chopping and second-order resonance TTV together constrain the mass of planet c and the pair's combined eccentricity, though the chopping TTV amplitude has a large uncertainty, with $1\, M_{\oplus *} \lesssim m_c \lesssim 8\, M_{\oplus *}$ at 1σ confidence. Consequently, the inferred masses are quite sensitive to the assumed priors.

Jontof-Hutter et al. (2015) measure masses $[m_b, m_c, m_d] = [0.13^{+0.12}_{-0.08}, 3.85^{+3.77}_{-2.30}, 1.28^{+1.36}_{-0.78}]\, M_{\oplus *}$ from MCMC analysis of transit data up to Quarter 14. Our default priors result in lower planet masses (Table 1) than inferred by Jontof-Hutter et al. (2015), who adopt priors that are uniform in planet masses and eccentricities. Our high-mass priors give close agreement with the masses found by Jontof-Hutter et al. (2015).

Kepler-177 b**, c** (Figure 9.27): Kepler-177 b's and c's mutual fundamental and chopping TTVs constrain the masses and combined eccentricity of the planet pair. Jontof-Hutter et al. (2016) analyze the TTVs of Kepler-177 b and c and find planet masses $[m_b, m_c] = [5.7 \pm 0.8, 14.6^{+2.7}_{-2.5}]\, M_{\oplus *}$, which agree well with our results: $[m_b, m_c] = [5.4 \pm 0.8, 13.3^{+2.4}_{-2.7}]\, M_{\oplus *}$. Jontof-Hutter et al. (2016) perform a second fit using an alternate set of transit times and find masses that are larger by more than 1σ for both planets.

Kepler-310 c, d* (Figure 9.28): Planet c's chopping and second-order resonance TTVs combine to constrain the mass of planet d and the pair's combined eccentricity. The nondetection of chopping in planet d's TTV gives an upper limit on planet c's mass that agrees well with the *N*-body results.

Kepler-345 b**, c** (Figure 9.29): The absence of chopping in Kepler-345 b's and c's TTVs places upper limits on their masses. Kepler-345 b and c are very near the fourth-order 19:15 MMR, with $|15P_c/19P_b - 1| = 6 \times 10^{-4}$. We fit Kepler-345 b's and c's TTVs with an analytic MCMC fit that, in addition to the fundamental, second-harmonic, and chopping TTVs, includes the effects of the 19:15 MMR on each planet's TTV.[8] By comparing the results of analytic MCMC fits with and without the effects of 19:15 MMR terms included, we find that these terms are crucial for constraining the maximum value of the planet pairs' combined eccentricity.

Kepler-359 c**, d** (Figure 9.30): Kepler-359 c's and d's mutual chopping TTVs constrain both planets' masses. The best-fit periods place the planet pair quite near the 4:3 MMR ($\Delta = -0.002$). Because of Kepler-359 c's and d's proximity to resonance, their transit time observations cover a relatively short portion of the super-period of their fundamental TTVs. As a result, there is a strong covariance between the planets' precise periods and their fundamental TTV amplitudes, which complicates the application of our analytic formulae. Constraints from the fundamental TTV have been omitted in Figure 9.30.

Kepler-444 b, c, d**, e***, f* (Figures 9.31–9.34): Kepler-444 is a compact five-planet system with each adjacent pair of planets near a first-order mean MMR. Campante et al. (2015) validate the planetary nature of the system and measure a precise stellar age of 11.2 ± 1.0 Gyr via astroseismology. Planets b/c are near a 5:4 MMR, c/d are near a 4:3 MMR, d/e are near or in a 5:4 MMR, and e/f are near a 5:4 MMR. None of the planets' TTVs show large variations. The planets' lack of chopping TTVs place stringent upper limits on their masses. The masses of planets d and e are robust to the choice of priors. Their masses and combined eccentricity are consistent with the fundamental and chopping constraints, though no upper bound on their eccentricity is apparent from the analytic constraints. The planet pair is very near resonance ($\Delta = 0.001$), where the assumptions of the analytic model start to break down. Their extreme proximity to resonance likely plays a role in limiting the maximum combined eccentricity consistent with their TTVs.

Kepler-526 b, 02 (Figure 9.35): Kepler-526 b and 02 are near a 5:4 MMR. Planet b does not induce any detectable TTV in Kepler-526.02. Lack of chopping TTVs provides upper limits on the masses of Kepler-526 b and 02.

Kepler-549 01, b* (Figure 9.36): The masses of Kepler-549.01 and b are constrained by their mutual chopping components, especially planet b's mass. The planets lack of TTV from the nearby 5:3 MMR ($\Delta = 0.047$) places a loose upper bound on their combined eccentricity (not shown in Figure 9.36). The *N*-body posterior shown in Figure 9.36 is confined to significantly smaller combined eccentricities than the upper bound derived from the lack of a 5:3 MMR signal. Kepler-549 01/b are very near the third-order 7:4 MMR ($\Delta = -0.003$), and this likely plays a role in further constraining the eccentricities of the planet pair.

A.2. Second Harmonic Systems

Kepler-23 b, c, d (Figures 9.37–9.38): Kepler-23 b and c are near the 3:2 MMR and have strong fundamental TTVs. The constraints from their mutual interactions are summarized in Figure 9.37. The planet's second-harmonic TTV constraints appear to be in tension with each other: the constraint in the right panel (planet b's TTV) favors large $|\mathcal{Z}|$ values that are ruled out by the left panel constraint (planet c's TTV). The right-hand panel second-harmonic TTV constraint is consistent with 0 at the 1.5σ level. We use an analytic MCMC fit to further investigate the discrepancy between the two constraints. The analytic MCMC combines the constraints of both planets' TTVs simultaneously so that the stronger of the two conflicting second-harmonic TTV constraints will dictate the inferred

[8] Terms in the analytic TTV formulae accounting for the fourth-order 19:15 MMR are derived by a straightforward extension of the derivation in Paper I (see also Deck & Agol 2016).

solution. The analytic MCMC results in Figure 9.37 demonstrate that the combination of both planets' TTV constraints gives good agreement with the *N*-body results.

The constraints from planet c's and d's mutual TTVs are summarized in Figure 9.38. Planets c and d are near the 7:5 MMR but do not induce significant second-order resonance TTVs in each other. Planet c's mass inferred with the default prior MCMC is somewhat smaller than the mass inferred from the chopping constraint, indicating that the higher prior probability assigned to lower masses by the default prior outweighs the likelihood contribution of the chopping TTV.

Kepler-24 b, c, e (Figures 9.39–9.40): Constraints from planet b's and c's interactions are summarized in Figure 9.39. The second-harmonic TTV constraint in the bottom left panel (from planet c's TTV) sets a lower limit on $|\mathcal{Z}|$. The planet masses are not strongly constrained, and their inferred masses are sensitive to the assumed priors. Planet e does not induce any detectable TTV in planet c, and the interactions of planet c and e are not very constraining.

Kepler-24 hosts an additional planet, d, with a radius of $1.7R_\oplus$ on a 4.2-day orbit somewhat near the 2:1 MMR with planet c. Planet d shows no significant TTV. We conducted *N*-body MCMC fits including planet d and find no significant difference in the posterior distributions of the parameters of planets b, c, and e. Our stability tests find that $\sim$10% of the initial conditions (53/500) drawn from the default posterior for Kepler-24 are unstable. The unstable posterior points are shown in Figures 9.39 and 9.40. The unstable points have slightly higher combined eccentricities relative to the overall posterior distribution, but given their modest difference and relatively low occurrence, we do not attempt to correct our posteriors to account for stability.

Kepler-27 03, b, c (Figure 9.41): In addition to large fundamental TTVs, planets b and c have nonzero second-harmonic TTVs at 1σ significance. The constraints from the second-harmonic TTV cannot easily be plotted in the $\mu - |\mathcal{Z}|$ plane because of the indirect terms in the analytic formulae for planets near the 2:1 MMR (see Paper I). Instead, we illustrate the contribution of the second-harmonic TTV to constraining planet parameters by including in Figure 9.41 the results of an MCMC fit using the analytic formulae. The analytic MCMC shows fair agreement, though it favors slightly larger eccentricities and smaller masses than the full *N*-body fit. The Kepler-27 system hosts an additional (candidate) planet, KOI-0841.03, interior to planets b and c that does not lie near any low-order resonances or exhibit any significant TTVs. We include KOI-0841.03 in our *N*-body MCMC fits but find that its properties are largely unconstrained.

Kepler-28 b, c (Figure 9.42): Neither Kepler-28 b nor c has a significant second-harmonic TTV. The absence of second-harmonic TTVs imposes an upper bound of $|\mathcal{Z}| \lesssim 0.1$ on their combined eccentricity. A lack of chopping places a 1σ upper bound $m_c \lesssim 7\, M_{\oplus *}$ on the mass of planet c.

Kepler-54 b, c (Figure 9.43): Kepler-54 b and c show strong fundamental TTVs caused by their proximity to the 3:2 MMR. Figure 9.43 indicates that the two planets' second-harmonic TTVs give conflicting constraints. To determine which of the conflicting constraints more strongly influences the likelihood of inferred planet parameters, we fit the TTVs of both planets simultaneously with an analytic MCMC. Analytic MCMC results, shown in purple in Figure 9.43, demonstrate that simultaneous fitting of both TTVs gives good agreement with the *N*-body results.

Kepler-56 b, c** (Figure 9.44): Kepler-56 b and c are near a 2:1 MMR. Planet b's second-harmonic TTV amplitude is nonzero at $>2\sigma$ significance. As with Kepler-27 above, we include results from an analytic MCMC fit to illustrate the constraints contributed by the second-harmonic TTV. The analytic MCMC shows good agreement with the *N*-body results.

Huber et al. (2013) previously analyzed the Kepler-56 system, fitting 10 RV measurements plus a full "photodynamical" model fit directly to the *Kepler* light curve. Huber et al. (2013) measure masses $[m_b, m_c] = [22.1^{+3.9}_{-3.6}, 181^{+21}_{-19}]\, M_\oplus$, consistent with our MCMC results in Table 1.

Kepler-89 c, d** (Figure 9.45): Both Kepler-89 c and d have nonzero second-harmonic TTVs at $>1\sigma$ significance. Figure 9.45 shows the constraints from the planets' fundamental TTVs along with the results of an analytic MCMC that includes second-harmonic TTV terms. The analytic MCMC shows good agreement with the *N*-body posteriors, demonstrating that the second-harmonic signals break the mass/eccentricity degeneracy for this system. Kepler-89 hosts two additional planets, b and e, excluded from our analysis because their periods place them well away from any low-order MMRs with planets c and d.

Kepler-89 c and d are among the few planets for which both RV and TTV mass measurements have been reported, with RV mass measurements reported by both Hirano et al. (2012) and Weiss et al. (2013) and a previous TTV measurement reported by Masuda et al. (2013). The masses fit by both Masuda et al. (2013) and Hirano et al. (2012) (who measure the mass of planet d only) agree well with the results of our TTV analysis. Weiss et al. (2013) find $m_d = 106 \pm 11\, M_\oplus$, in tension with our determination of planet d's mass even if we adopt their best-fit stellar mass, $M_* = 1.3\, M_\odot$.

Kepler-114 b, c, d (9.46–9.47): Kepler-114 is a three planet system with both the inner pair (b/c) and outer pair (c/d) of planets near 3:2 MMRs. Interactions between b and c, summarized in Figure 9.46, do not provide strong constraints.

Figure 9.47 summarizes the interactions of the c/d pair. Planet c does not induce any significant TTV in planet d. The bottom left panel shows a strong fundamental TTV constraint (from planet d's TTV), but the chopping and second-harmonic TTV amplitudes are consistent with zero at the 1σ level. Results of an analytic MCMC are included in Figure 9.47. We find, by turning on and off the contribution of the chopping and second-harmonic TTVs separately in the analytic MCMC, that both components help constrain planet c's mass.

Kepler-122 e, f (Figure 9.48): Planet e's second-harmonic TTV and lack of chopping help break some of the mass–eccentricity degeneracy, constraining $|\mathcal{Z}| \lesssim 0.1$ and $m_f \lesssim 6\, M_{\oplus *}$. Our stability tests find 69 out of 500 of the *N*-body integrations initialized from the default posterior sample to be unstable. Figure 9.48 shows that the unstable initial conditions are distributed randomly throughout the full posterior, and dynamical stability considerations should not influence the inferred planet masses and combined eccentricities.

Kepler-279 c, d** (Figure 9.49): Kepler-279 c and d both have significant ($>3\sigma$) nonzero second-harmonic TTVs, and the combined constraints of the planets' fundamental and second-harmonic TTVs break the mass–eccentricity degeneracy. The

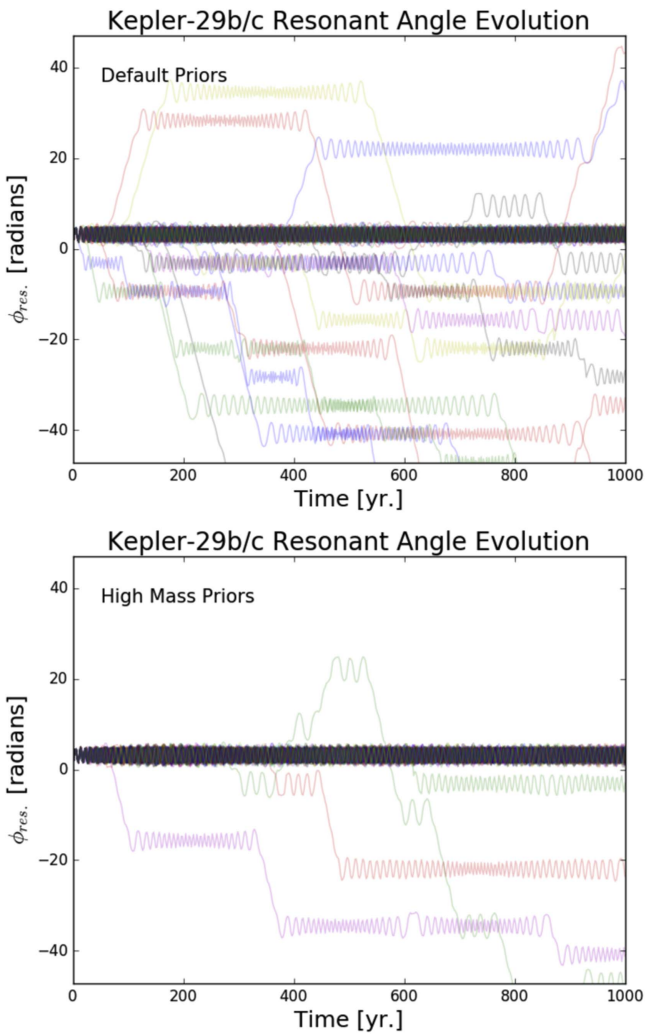

Figure 10. Top panel: time evolution of the Kepler-29 b/c 9:7 resonant angle for 100 random initial conditions drawn from the default posteriors. The resonant angle is defined as the complex phase of Equation (11). The resonant angles librate or alternate intermittently between libration and circulation. Alternating behavior is indicative of chaotic orbits. Note that the vertical axis extends beyond $\pm\pi$ to account for windings of resonant angles that circulate. Bottom panel: same as the top panel, but with initial conditions drawn from the high-mass posteriors.

inferred masses and combined eccentricity are not strongly affected by the choice of priors. Kepler-279 hosts a third planet, b, interior to planets c and d with a period of 12.3 days. Planet b's period places it far from planets c and d, and it is not expected to have an appreciable influence on either c's or d's TTV.

Kepler-396 b, c (Figure 9.50): Kepler-396 b's second-harmonic TTV amplitude is nonzero with $>2\sigma$ confidence. We include the results of an analytic MCMC in Figure 9.50 since second-harmonic TTV constraints cannot be visualized in the $\mu - |\mathcal{Z}|$ plane for planets near the 2:1 MMR. The analytic MCMC fit agrees well with the *N*-body results. Lack of chopping gives a 1σ upper bound of $m_c \lesssim 6\, M_{\oplus *}$ on planet c's mass.

A.3. Resonant and Massive Systems

Kepler-9 b, c** (Figure 9.51): Kepler-9 b and c are a pair of Saturn-sized planets near a 2:1 MMR. Both planets' masses and their combined eccentricity are measured quite precisely. Fits of Kepler-9 b's and c's TTV with the analytic formulae

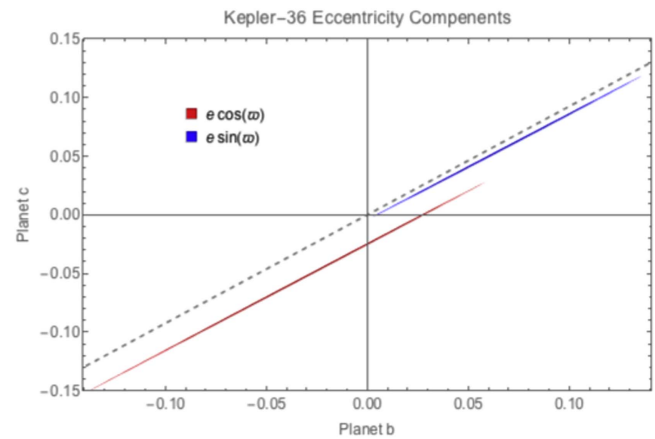

Figure 11. *N*-body MCMC posteriors for Kepler-36 b and c eccentricity components. The posterior distributions of $e_i \cos(\varpi_i)$ (red) and $e_i \sin(\varpi_i)$ (blue) for $i = b, c$ are plotted with 68% and 95% credible regions indicated by dark and light shading, respectively. The dashed line shows the expected correlation slope, $-f_{27}/f_{31} \approx 0.9$, for a constant value of $\mathcal{Z}$ (Equation (3)). The posterior shows a strong correlation in the direction expected from the analytic TTV formulae.

underpredict the masses found by *N*-body fitting by $\sim 10\, M_{\oplus *}$ for both planets. The analytic formulae fail to accurately recover the mass of Kepler-9 b and c because the formulae break down for planet pairs in or too near an MMR. The width of a first-order MMR, as measured in terms of Δ, scales as $\mu^{2/3}$ (e.g., Henrard & Lemaitre 1983), and Kepler-9 b's and c's large masses place them quite close to being in the 2:1 resonance. We find via *N*-body integrations that while the resonant angles $2\lambda_c - \lambda_b - \varpi_b$ and $2\lambda_c - \lambda_b - \varpi_c$ circulate for the best-fit masses of Kepler-9 b and c, increasing the masses by only $\sim$30% causes the angles to transition from circulation to libration.

Kepler-9 has been studied previously by multiple authors (Holman et al. 2010; Borsato et al. 2014; Dreizler & Ofir 2014). Both Borsato et al. (2014) and Dreizler & Ofir (2014) fit masses from TTV analysis that are $\sim$60% smaller than those found by Holman et al. (2010), who base their planet masses primarily on six RV observations.[9] The masses and eccentricities that we fit agree well with those determined by Borsato et al. (2014) and Dreizler & Ofir (2014). The source of disagreement between the TTV- and RV-derived masses is unclear, though, as the authors of both previous TTV studies note, the RV observation spans a short time baseline, less than an entire orbit of planet c, and follow-up RV observations could shed light on the discrepancy.

Kepler-29 b, c (Figure 9.52): Our *N*-body fits indicate that Kepler-29 b and c's are librating in the 9:7 MMR. The *N*-body MCMC results agree well with analytic constraints derived form the second-order resonance TTV despite the fact that the pair's libration in resonance violates the assumptions of the formulae's derivation (see Paper I). We confirm that Kepler-29 b and c are in the 9:7 MMR with a set of 100 *N*-body integrations using initial conditions drawn randomly from the MCMC posteriors. The *N*-body integrations are done with the REBOUND code's WHFast integrator (Rein & Tamayo 2015). Confirming that the planet pair is in resonance requires testing resonant angle(s) for

[9] Holman et al. (2010) also include a limited number of TTV observations spanning only $\sim$250 days in their fitting. They find that their TTV observations alone do not strongly constrain the planet masses.

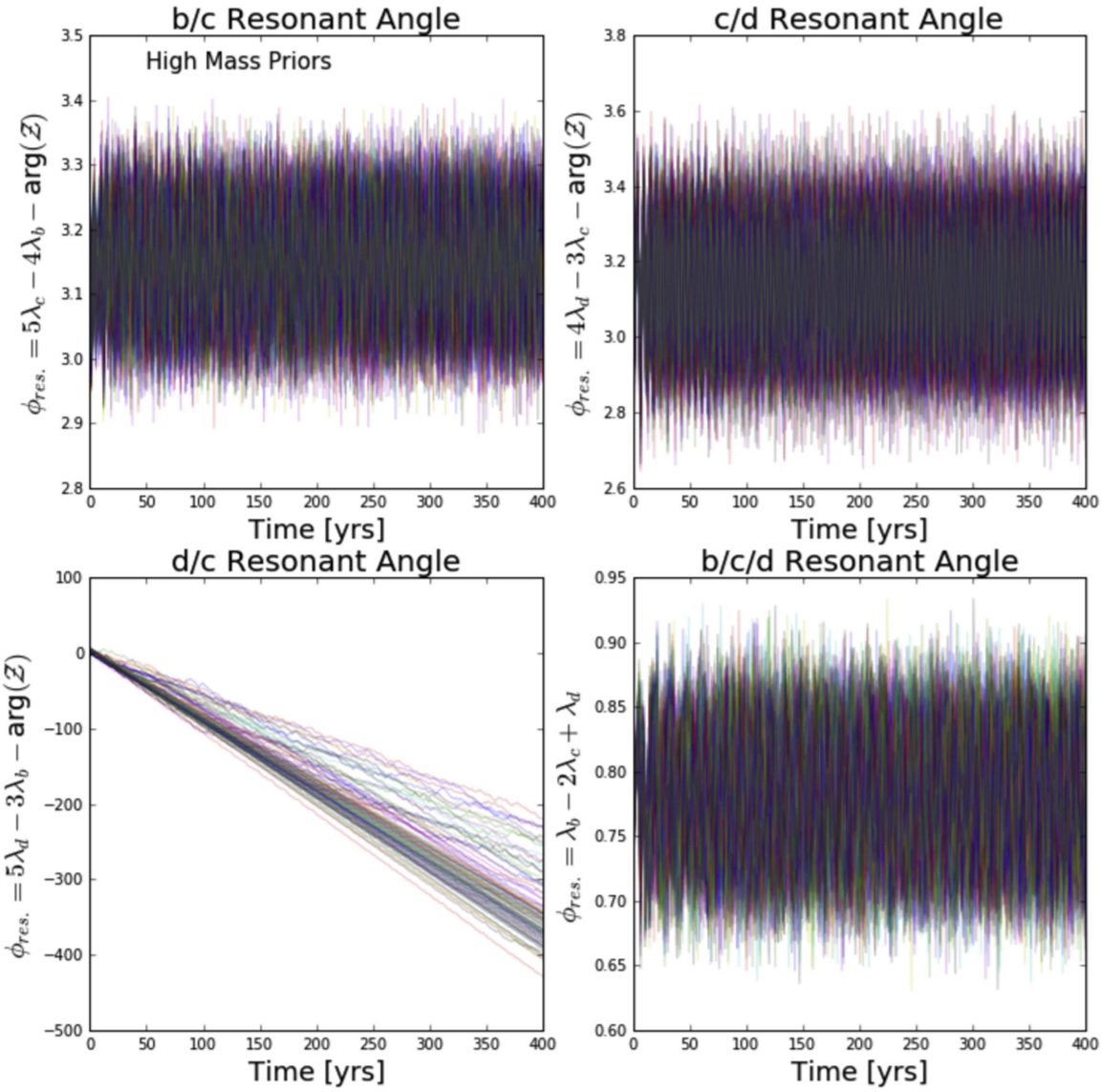

Figure 12. Resonant angle time evolution for the Kepler-60 system for 100 simulations with initial conditions randomly drawn from the high-mass MCMC posterior. Vertical axes are extended beyond $\pm\pi$ to account for windings of resonant angles that circulate.

libration. There are three resonant angles associated with a 9:7 MMR: $9\lambda_c - 7\lambda_b - 2\varpi_b$, $9\lambda_c - 7\lambda_b - \varpi_b - \varpi_c$, and $9\lambda_c - 7\lambda_b - 2\varpi_c$, each of which appears as a cosine term in the Laplacian expansion of the planets' disturbing function (Murray & Dermott 2000). The sum of the cosine terms can be written, to lowest order in eccentricities, in terms of the planets' complex eccentricities as

$$\frac{1}{2}(f_{45} z_b^{*2} + f_{53} z_c^{*2} + f_{49} z_b^* z_c^*) e^{i(9\lambda_c - 7\lambda_b)} + \text{c.c.}, \qquad (11)$$

where the f_i combinations of Laplace coefficients are as defined in Appendix B of Murray & Dermott (2000), the asterisk indicates complex conjugation, and "c.c." denotes the complex conjugate of the preceding term. Instead of testing each of the three possibly resonant angles separately, we plot the complex phase of the term preceding "c.c." in Equation (11) in Figure 10. Libration of this complex phase implies libration of at least one of the 9:7 MMR angles enumerated above. Figure 10 shows the time evolution of the resonant angle from N-body integrations drawn from both the default and high-mass posteriors. For all initial conditions, the resonant angle either librates or chaotically alternates between libration and circulation.[10]

Jontof-Hutter et al. (2016) and Migaszewski et al. (2017) also conduct an MCMC analysis of Kepler-29 b's and c's Q1–17 transit times. Our high-mass priors yield masses and error bars similar to theirs. Yet despite that, we do not consider this system as robust because the default and high-mass priors disagree.

Kepler-30 b, c** (Figure 9.53): Kepler-30 b and c are near a 2:1 MMR. The analytic TTV formulae are not expected to be accurate given Kepler-30 c's large mass ($m_c \approx 550\, M_{\oplus *}$). Sanchis-Ojeda et al. (2012) fit masses $[m_b, m_c] = [11.3 \pm 1.4,$

[10] We confirm the chaotic nature of the initial conditions that produce alternating evolution with the MEGNO chaos indicator (Cincotta et al. 2003) implemented in the REBOUND code.

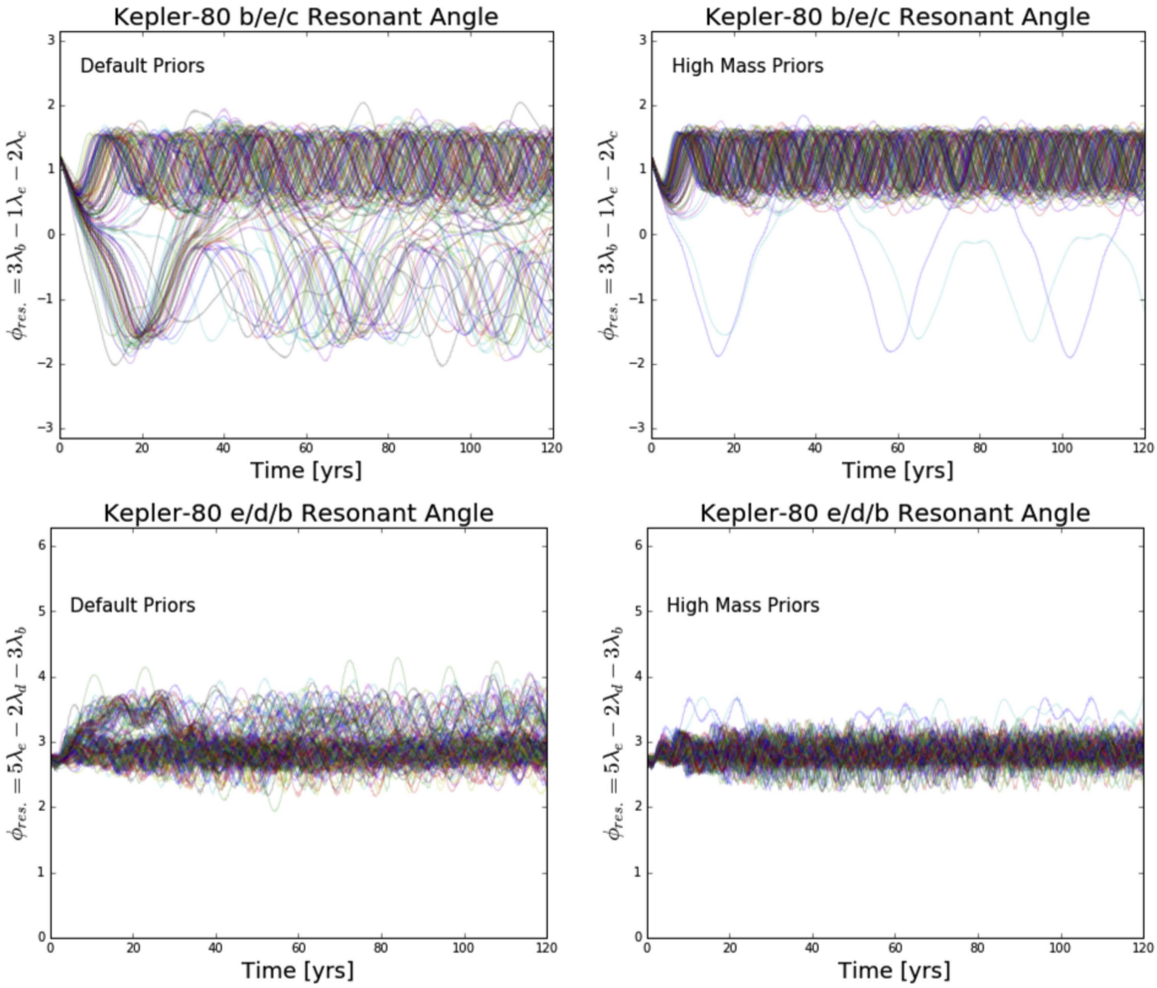

Figure 13. Resonant angle time evolution for the Kepler-80 system. The left panels show 100 random simulations with initial conditions drawn from the default posterior. The right panels show the same angles with initial conditions drawn from the high-mass posteriors.

640 ± 50] $M_{\oplus *}$ based on a TTV analysis of 2.5 yr of transit data. We find somewhat smaller masses than Sanchis-Ojeda et al. (2012), though our results are consistent within $\lesssim 2\sigma$. Our TTV analysis of Kepler-30 is based on the transit times computed by Holczer et al. (2016), who note that the transit times computed by Rowe et al. (2015) for Kepler-30 b are erroneous.

Kepler-36 b, c** (Figure 9.54): Kepler-36 b and c are near a 7:6 MMR ($\Delta = 0.005$). We omit any analysis of this system with the analytic formulae because they provide poor approximations to the planets' TTVs, due to both their extreme proximity and their small Δ. Despite the analytic model's poor performance, the planets' eccentricity vector components are still strongly correlated, as predicted by the analytic model. Figure 11 compares the eccentricity vector posteriors to the correlation predicted by the analytic model. Kepler-36 b's and c's eccentricities are poorly constrained by the TTVs, and only their combination, $\mathcal{Z}$, is measured accurately. Our analysis agrees with the previous TTV mass measurements of Kepler-36 b and c by Carter et al. (2012).

Kepler-60 b, c*, d** (Figures 9.55–9.56): The Kepler-60 planets are in a chain of MMRs. The inner b/c pair is in a 5:4 MMR, and the outer c/d pair is in a 4:3 MMR.[11] This configuration placed the b/d pair near a 5:3 MMR. Furthermore, the planets are in or near a three-body resonance satisfying $|n_b - 2n_c + n_d| \approx 0$. Figures 9.55 and 9.56 show that the default and high-mass posterior samples occupy disjoint regions of parameter spaces. This indicates that the likelihood function defined by the TTV observations has multiple local maxima of similar likelihood, and each prior weights more toward a different maximum. Nearly all (489/500) of the Kepler-60 default posterior points integrated in our stability tests are unstable. We therefore conclude that the high-mass posteriors more accurately reflect the true planet properties. For Kepler-60 only, we use the high-mass posteriors instead of the default posteriors to compute the masses, densities, and envelope fractions plotted of the figures in the body of the paper, though we still report default posterior results in Tables 1 and 2.

Figure 12 examines the time evolution of the resonant angles of each first-order MMR and the three-body resonance. For each planet pair near a j:$j-1$ MMRs, Figure 12 plots the resonant angles

$$\phi_{res.} = j\lambda' - (j-1)\lambda - \arg(\mathcal{Z}), \tag{12}$$

where λ and λ' are the mean anomalies of the inner and outer planet, respectively. The dynamics of a first-order resonance can be shown to depend only on this single resonant angle (e.g., Batygin & Morbidelli 2013). We plot resonant angle

[11] The resonant angles of Kepler-60 b/c and c/d undergo libration. Strictly speaking, "in resonance" also implies the existence of a separatrix in phase space (e.g., Henrard & Lemaitre 1983). Deducing the existence of a separatrix requires a more detailed dynamical analysis, beyond the scope of this work.

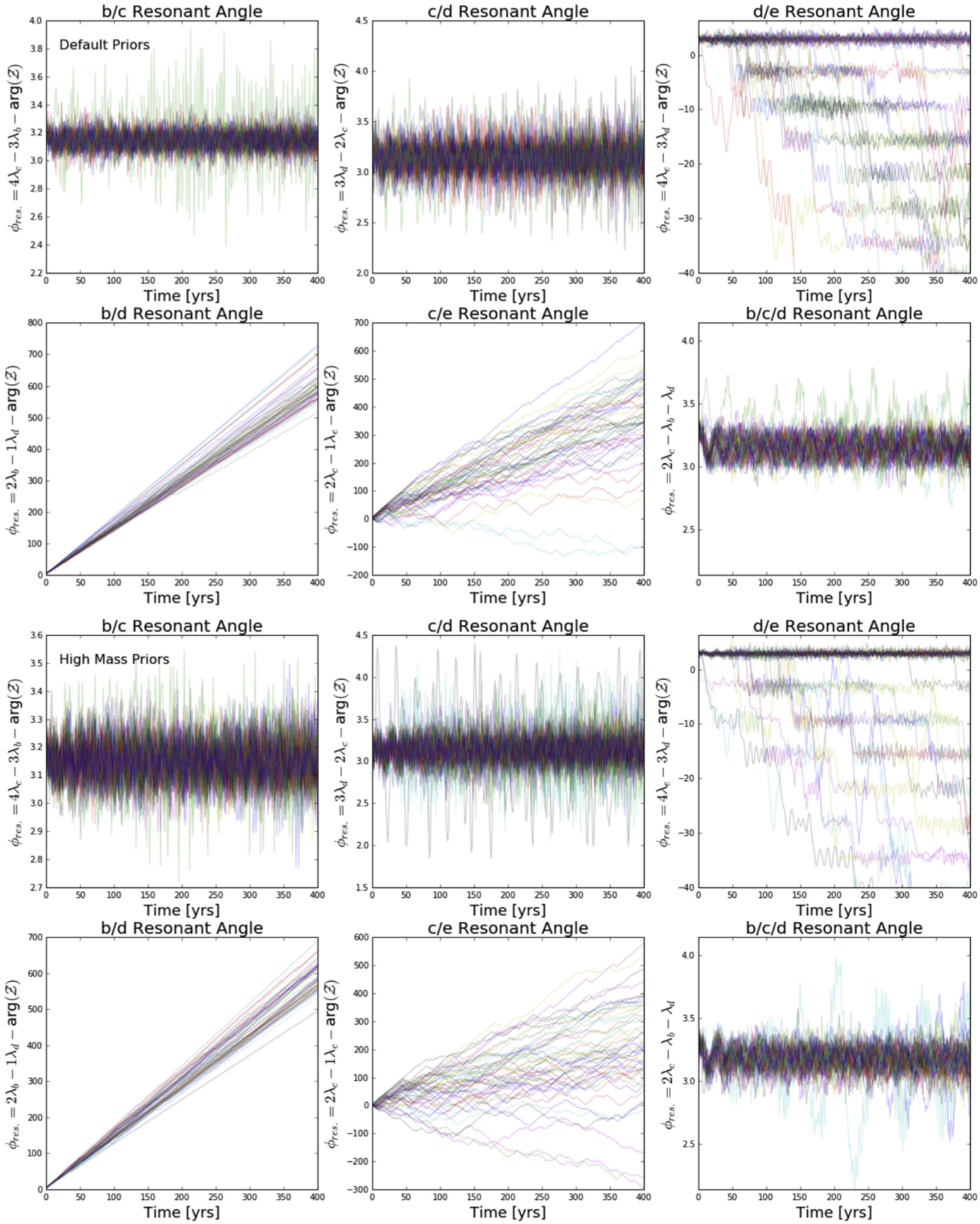

Figure 14. Resonant angle time evolution for the Kepler-223 system. The top two rows show the time evolution for initial conditions drawn from the default posterior. The bottom two rows show the time evolution of the same angles for initial conditions drawn form the high-mass posterior. Vertical axes are extended beyond $\pm\pi$ to account for windings of resonant angles that circulate.

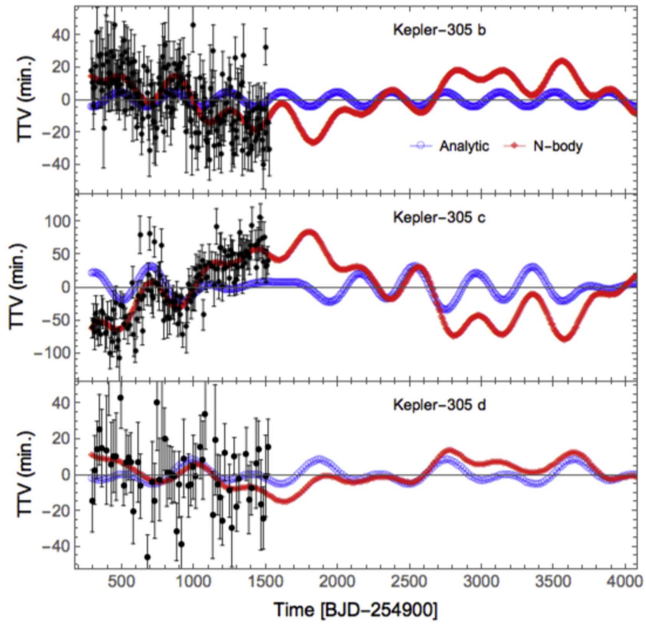

Figure 15. TTVs of the outer three planets of the Kepler-305 system. The observed data are shown as black points. The best-fit *N*-body and analytic solutions are shown in red and blue, respectively, and are plotted beyond the time baseline covered by the observed data. The *N*-body solution shows a long-term variability not captured by the best-fit analytic solution.

evolution for initial conditions drawn from the high-mass posteriors only, since the default posteriors produce rapidly unstable configurations.

The high-mass prior MCMC results (Table 1) agree well with the masses measured by the two previous studies of Goździewski et al. (2016) and Jontof-Hutter et al. (2016). Both Goździewski et al. (2016) and Jontof-Hutter et al. (2016) find similar values for the masses of the Kepler-60 system. We find that the three-body resonance angle, $\lambda_b - 2\lambda_c + \lambda_d$, librates for all initial conditions drawn from the MCMC posterior computed with the high-mass prior. Jontof-Hutter et al. (2016) find that 20% of the posterior samples they test have a three-body resonance angle that circulates while the system remains stable for at least 1 Myr.

Kepler-80 d, e*, b, c* (Figures 9.57–9.60): The planets of Kepler-80 are arranged in a complex chain of resonances. Each adjacent pair is near a first-order MMR, starting with the d/e pair near a 3:2 MMR, followed by the e/b pair near a 3:2 MMR, and finally the b/c pair near a 4:3 MMR. Additionally, the second and fourth planets, e and c, are near a 2:1 MMR. Based on *N*-body integrations initialized from our MCMC posteriors, all the resonant angles associated with these first-order MMRs circulate. Three-body resonances occur when the frequencies of two two-body resonance angles are equal and the circulation rates of each two-body resonant angle in the Kepler-80 system are nearly equal, i.e., $3n_e - 2n_d \approx 3n_b - 2n_e \approx 4n_c - 3n_b$. The two three-body resonance angles,

$$\phi_{e,d,b} = 5\lambda_e - 2\lambda_d - 3\lambda_b, \tag{13}$$

$$\phi_{b,e,c} = 3\lambda_b - \lambda_e - 2\lambda_c, \tag{14}$$

librate in the Kepler-80 system. Figure 13 plots the time evolution of the resonant angles, Equations (13) and (14), computed by *N*-body integrations initialized from the MCMC posterior distributions. Each angle librates for every initial condition that we integrate.

Because of the three-body resonances, planets e, b, and c have multiple fundamental TTVs with the same super-period. Planet e, for example, has fundamental TTVs induced by its proximity to the 3:2 MMRs with both planet d and b, both with super-periods of ∼192 days. Multiple fundamental TTVs with the same frequency inhibit our linear fitting procedure for generating constraint plots since the sinusoidal basis functions used to fit fundamental TTVs are not independent. To illustrate the constraints of the analytic model in Figures 9.57–9.60, we perform an MCMC that uses the analytic formulae to fit the planets' TTVs directly, as opposed to fitting amplitudes measured by a least-squares fit. The results of the analytic MCMC in Figures 9.57–9.60 show fair agreement for planets b and c but suggest that planet d's and e's masses are consistent with 0, at odds with the *N*-body results.

Least-squares fits to the transit times of planets b and c (and to a lesser extent planet e) are significantly improved by allowing for a quadratic trend in the TTVs. We suspect that this long-term quadratic trend arises from the dynamical influence of the three-body resonances on the TTVs and contributes to the robust constraints for planet d's and e's masses found via *N*-body MCMC.

MacDonald et al. (2016) recently conducted a TTV analysis of the Kepler-80 system. Their mass determinations for the robustly constrained planets d and e are consistent with ours within 1σ uncertainties after accounting for their use of a somewhat larger stellar mass of $M_* = 0.73 \pm 0.02\,M_\odot$ compared to our $M_* = 0.6 \pm 0.03\,M_\odot$.

Kepler-223 b, c*, d*, e* (Figures 9.61–9.63): The periods of the Kepler-223 planets place each successive adjacent pair of planets in or near a first-order MMR with a 4:3 MMR between b and c, a 3:2 MMR between c and d, and a 4:3 MMR between d and e. We test for resonant angle librations in the Kepler-223 system with *N*-body integrations. The top row of Figure 14 plots the resonant angles of each adjacent planet pair. The resonant angles of the pairs b/c and c/d librate over the entire 400 yr integration. The d/e resonant angle librates for 23 of the 50 simulations, while in the other 27 simulations it alternates chaotically between libration and circulation. The left two panels of the bottom row show the 2:1 MMR resonance for planets b/d and c/e, respectively, both of which circulate. Finally, the bottom right panel of Figure 14 shows that the three-body resonant angle $2\lambda_c - \lambda_b - \lambda_d$ librates about π for all initial conditions. We do not apply the analytic TTV formulae to the Kepler-223 system since they are not expected to accurately represent the TTVs of planets librating in resonance.

A sizable number (164/500) of the stability test *N*-integrations initialized from the default posterior sample are found to be unstable on a short timescale. These unstable posterior samples are plotted in Figures 9.61–9.63 as red points. The distribution of unstable initial conditions is not obviously distinct from the overall posterior distribution in terms of combined eccentricities and planet masses. Therefore, we do not attempt to account for stability considerations in our reported mass and combined eccentricity measurements for the Kepler-223 system.

Mills et al. (2016) infer masses $[m_b, m_c, m_d, m_e] = [7.4^{+1.3}_{-1.1}, 5.1^{+1.7}_{-1.1}, 8.0^{+1.5}_{-1.3}, 4.8^{+1.4}_{-1.2}]\,M_\oplus$ from a TTV analysis of the Kepler-223 system's Q1–17 transit times. Their results

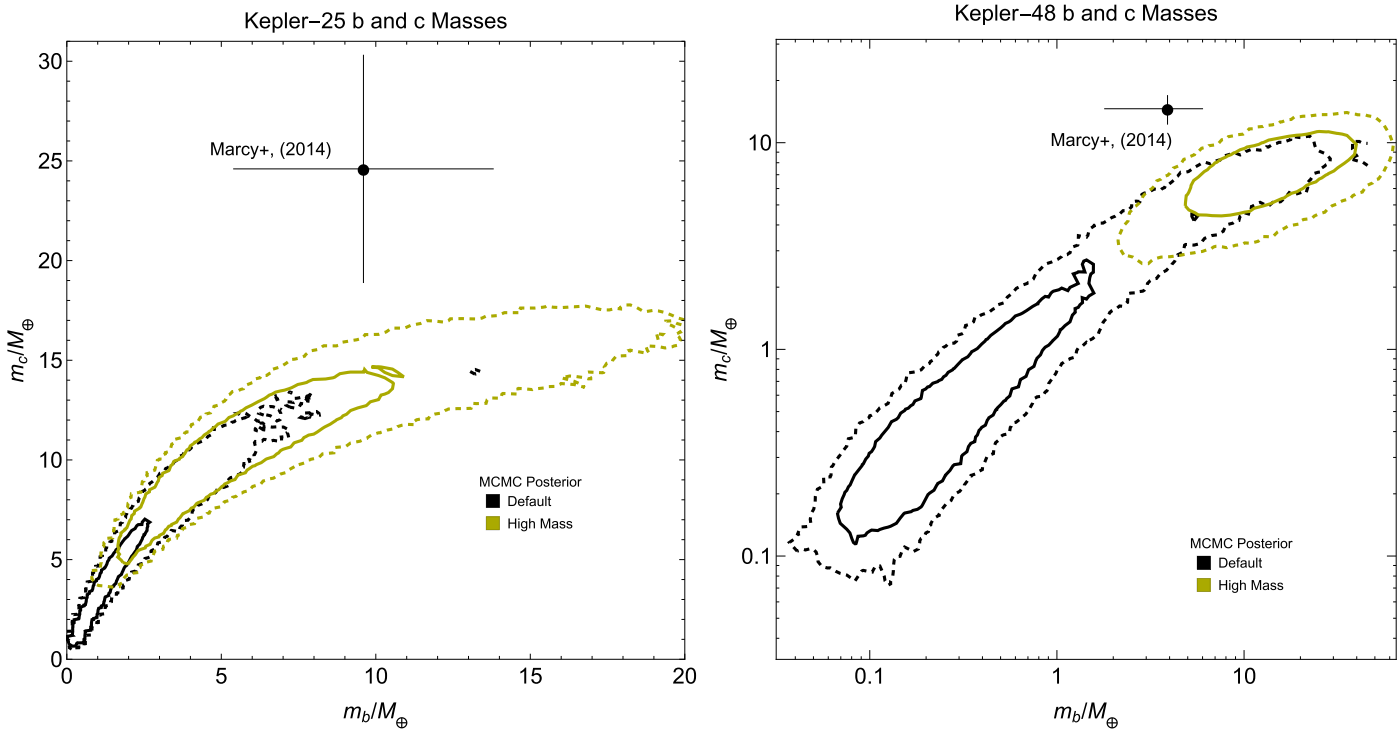

Figure 16. Contours show 68% (solid) and 95% (dashed) credible regions in planet mass from the default (black) and high-mass (yellow) *N*-body MCMC posteriors for Kepler-25 and Kepler-48. The black points with error bars show the RV measurements of Marcy et al. (2014). The planet–star mass ratios from the *N*-body MCMC posteriors have been multiplied by the best-fit stellar masses, $M_* = 1.19\,M_\odot$ (Kepler-25) and $M_* = 0.88\,M_\odot$ (Kepler-48), found by Marcy et al. (2014).

roughly agree with ours; the measurement of m_c is the most in tension (2.4σ). Furthermore, our TTV fit gives only an upper bound for m_e, but the upper limit from the high-mass prior fit is consistent with the m_e fit by Mills et al. (2016).

Kepler-305 03, b, c, d** (Figures 9.64–9.66): Kepler-305 b and c are near a 3:2 MMR, and planets c and d are near a 2:1 MMR. The inferred masses and eccentricities agree well with the constraints of the measured fundamental TTVs of planets b, c, and d. The masses of planets c and d are classified as robust based on the *N*-body MCMC results, though the analytic constraints shown in Figure 9.66 do not reveal what is responsible for breaking the mass–eccentricity degeneracy. Figure 15 shows that the *N*-body TTV solution exhibits a clear long-term variability not captured by the analytic model. We are unable to identify the origin of this variability after searching unsuccessfully for higher-order MMRs and three-body resonances among the planets. Both the b/c and c/d pairs are fairly close to resonance ($\Delta = 0.007$ and $\Delta = 0.009$, respectively), and the variability could possibly be caused by resonance effects not captured in the analytic model. We speculate that the dynamical origin of the long-term variability breaks the mass–eccentricity degeneracy for this system.

A.4. Degenerate Systems

A number of the TTV systems we analyze exhibit strong mass–eccentricity degeneracy. The constraint plots are shown for each degenerate system: Kepler-25, Kepler-31, Kepler-32, Kepler-48, Kepler-52, Kepler-53, Kepler-57, Kepler-176, Kepler-238, Kepler-277, Kepler-324, and Kepler-1126 in Figures 9.67–9.83. Our stability tests find a somewhat significant fraction of unstable initial conditions in the default posterior samples of Kepler-1126 (50/500). Figure 9.83 shows that the unstable initial conditions are distributed roughly randomly throughout the full posterior. Therefore, dynamical stability considerations should not influence the inferred planet masses and combined eccentricities.

Jontof-Hutter et al. (2016) also analyze the TTVs of Kepler-57 b and c and similarly find that the planets' masses and eccentricities are poorly constrained by the TTVs.

Marcy et al. (2014) measure RV planet masses for two of the degenerate systems, Kepler-25 b and c ($[m_b, m_c] = [9.6 \pm 4.2, 24.6 \pm 5.7]\,M_\oplus$) and Kepler-48 b and c ($[m_b, m_c] = [3.9 \pm 2.1, 14.6 \pm 2.3]\,M_\oplus$). The Marcy et al. (2014) mass measurements are inconsistent with the TTVs of both the Kepler-25 and Kepler-48 systems. Despite the fact that the TTVs suffer strong mass–eccentricity degeneracies, the fundamental TTVs constrain the planets' mass ratios in both systems. Figure 16 compares the RV mass measurements of Marcy et al. (2014) with the *N*-body MCMC posteriors for Kepler-25 and Kepler-48 systems. In both systems, Marcy et al. (2014) find outer planet masses that are larger than the TTV observations support. It is unclear which mass constraints are correct: it is possible that unmodeled effects, such as additional planets, contaminate the TTV, but it is also possible that the RV measurements are in error. Marcy et al. (2014) report additional planets at distant orbital separations in both the Kepler-25 and Kepler-48 systems. Kepler-25 hosts a nontransiting $\sim 90\,M_\oplus$ planet with a period of 123 days, and Kepler-48 hosts an additional transiting $\sim 8\,M_\oplus$ planet on a $\sim$43-day orbit, as well as a nontransiting $\sim 2\,M_J$ planet on a $\sim$1000-day orbit. We confirm via *N*-body calculations that these additional planets have negligible effects on the TTVs of Kepler-25 b/c and Kepler-48 b/c, as expected given their large orbital separations.

References

Agol, E., & Deck, K. 2016, ApJ, 818, 177
Agol, E., Steffen, J., Sari, R., & Clarkson, W. 2005, MNRAS, 359, 567
Alonso, R., Moutou, C., Endl, M., et al. 2014, A&A, 567, A112

Azzalini, A. 1985, J. Stat., 12, 171
Bakos, G. A., Torres, G., Pál, A., et al. 2010, ApJ, 710, 1724
Barros, S. C. C., Almenara, J. M., Deleuil, M., et al. 2014, A&A, 569, A74
Batygin, K., & Morbidelli, A. 2013, A&A, 556, A28
Berta-Thompson, Z. K., Irwin, J., Charbonneau, D., et al. 2015, Natur, 527, 204
Bodenheimer, P., & Lissauer, J. J. 2014, ApJ, 791, 103
Bordé, P., Bouchy, F., Deleuil, M., et al. 2010, A&A, 520, A66
Borsato, L., Marzari, F., Nascimbeni, V., et al. 2014, A&A, 571, A38
Borucki, W. J., Koch, D., Basri, G., et al. 2010, Sci, 327, 977
Borucki, W. J., Koch, D. G., Basri, G., et al. 2011, ApJ, 736, 19
Campante, T. L., Barclay, T., Swift, J. J., et al. 2015, ApJ, 799, 170
Carter, J. A., Agol, E., Chaplin, W. J., et al. 2012, Sci, 337, 556
Cincotta, P. M., Giordano, C. M., & Simó, C. 2003, PhyD, 182, 151
Cochran, W. D., Fabrycky, D. C., Torres, G., et al. 2011, ApJS, 197, 7
Dai, F., Winn, J. N., Arriagada, P., et al. 2015, ApJL, 813, L9
Dawson, R. I., & Johnson, J. A. 2012, ApJ, 756, 122
Deck, K. M., & Agol, E. 2015, ApJ, 802, 116
Deck, K. M., & Agol, E. 2016, ApJ, 821, 96
Dreizler, S., & Ofir, A. 2014, arXiv:1403.1372D
Dressing, C. D., Charbonneau, D., Dumusque, X., et al. 2015, ApJ, 800, 135
Dumusque, X., Bonomo, A. S., Haywood, R. D., et al. 2014, ApJ, 789, 154
Espinoza, N., Brahm, R., Jordán, A., et al. 2016, ApJ, 830, 43
Esteves, L. J., De Mooij, E. J. W., & Jayawardhana, R. 2015, ApJ, 804, 150
Fabrycky, D. C., Ford, E. B., Steffen, J. H., et al. 2012, ApJ, 750, 114
Fabrycky, D. C., Lissauer, J. J., Ragozzine, D., et al. 2014, ApJ, 790, 146
Fortney, J. J., Marley, M. S., & Barnes, J. W. 2007, ApJ, 659, 1661
Fressin, F., Torres, G., Charbonneau, D., et al. 2013, ApJ, 766, 81
Gaidos, E., & Mann, A. W. 2012, ApJ, 762, 41
Gautier, T. N. I., Charbonneau, D., Rowe, J. F., et al. 2012, ApJ, 749, 15
Gettel, S., Charbonneau, D., Dressing, C. D., et al. 2016, ApJ, 816, 95
Gilliland, R. L., Marcy, G. W., Rowe, J. F., et al. 2013, ApJ, 766, 40
Ginzburg, S., Schlichting, H. E., & Sari, R. 2016, ApJ, 825, 29
Goździewski, K., Migaszewski, C., Panichi, F., & Szuszkiewicz, E. 2016, MNRAS, 455, L104
Hadden, S., & Lithwick, Y. 2014, ApJ, 787, 80
Hadden, S., & Lithwick, Y. 2016, ApJ, 828, 44
Harpsøe, K. B. W., Hardis, S., Hinse, T. C., et al. 2013, A&A, 549, A10
Hartman, J. D., Bakos, G. A., Kipping, D. M., et al. 2011, ApJ, 728, 138
Henrard, J., & Lemaitre, A. 1983, CeMec, 30, 197
Hirano, T., Narita, N., Sato, B., et al. 2012, ApJL, 759, L36
Hogg, D. W., Myers, A. D., & Bovy, J. 2010, ApJ, 725, 2166
Holczer, T., Mazeh, T., Nachmani, G., et al. 2016, ApJS, 225, 9
Holman, M. J. 2005, Sci, 307, 1288
Holman, M. J., Fabrycky, D. C., Ragozzine, D., et al. 2010, Sci, 330, 51
Howe, A. R., Burrows, A., & Verne, W. 2014, ApJ, 787, 173
Huber, D., Carter, J. A., Barbieri, M., et al. 2013, Sci, 342, 331
Ikoma, M., & Hori, Y. 2012, ApJ, 753, 66
Jontof-Hutter, D., Ford, E. B., Rowe, J. F., et al. 2016, ApJ, 820, 39
Jontof-Hutter, D., Lissauer, J. J., Rowe, J. F., & Fabrycky, D. C. 2014, ApJ, 785, 15
Jontof-Hutter, D., Rowe, J. F., Lissauer, J. J., Fabrycky, D. C., & Ford, E. B. 2015, Natur, 522, 321
Kass, R. E., & Raftery, A. E. 2012, J. Am. Stat. Assoc., 90, 773
Kipping, D. M. 2014, MNRAS, 440, 2164
Kostov, V. B., McCullough, P. R., Carter, J. A., et al. 2014, ApJ, 784, 14
Lee, E. J., & Chiang, E. 2016, ApJ, 817, 90
Lissauer, J. J., Fabrycky, D. C., Ford, E. B., et al. 2011a, Natur, 470, 53
Lissauer, J. J., Jontof-Hutter, D., Rowe, J. F., et al. 2013, ApJ, 770, 131
Lissauer, J. J., Ragozzine, D., Fabrycky, D. C., et al. 2011b, ApJS, 197, 8
Lithwick, Y., Xie, J., & Wu, Y. 2012, ApJ, 761, 122
Lopez, E. D., & Fortney, J. J. 2014, ApJ, 792, 1
Lopez, E. D., Fortney, J. J., & Miller, N. 2012, ApJ, 761, 59
MacDonald, M. G., Ragozzine, D., Fabrycky, D. C., et al. 2016, AJ, 152, 105
Marcy, G. W., Isaacson, H., Howard, A. W., et al. 2014, ApJS, 210, 20
Masuda, K. 2014, ApJ, 783, 53
Masuda, K., Hirano, T., Taruya, A., Nagasawa, M., & Suto, Y. 2013, ApJ, 778, 185
Migaszewski, C., Goździewski, K., & Panichi, F. 2017, MNRAS, 465, 2366
Migaszewski, C., Słonina, M., & Goździewski, K. 2012, MNRAS, 427, 770
Mills, S. M., Fabrycky, D. C., Migaszewski, C., et al. 2016, Natur, 533, 509
Moutou, C., Almenara, J. M., Díaz, R. F., et al. 2014, MNRAS, 444, 2783
Murray, C. D., & Dermott, S. F. 2000, Solar System Dynamics (Cambridge: Cambridge Univ. Press)
Nesvorný, D. 2009, ApJ, 701, 1116
Nesvorný, D., Kipping, D., Terrell, D., et al. 2013, ApJ, 777, 3
Nesvorný, D., & Morbidelli, A. 2008, ApJ, 688, 636
Nesvorný, D., & Vokrouhlický, D. 2014, ApJ, 790, 58
Nesvorný, D., & Vokrouhlický, D. 2016, ApJ, 823, 72
Owen, J. E., & Wu, Y. 2013, ApJ, 775, 105
Pepe, F., Cameron, A. C., Latham, D. W., et al. 2013, Natur, 503, 377
Petigura, E. A., Howard, A. W., & Marcy, G. W. 2013, PNAS, 110, 19273
Rein, H., & Tamayo, D. 2015, MNRAS, 452, 376
Rogers, L. A. 2015, ApJ, 801, 41
Rogers, L. A., Bodenheimer, P., Lissauer, J. J., & Seager, S. 2011, ApJ, 738, 59
Rowe, J. F., Bryson, S. T., Marcy, G. W., et al. 2014, ApJ, 784, 45
Rowe, J. F., Coughlin, J. L., Antoci, V., et al. 2015, ApJS, 217, 16
Sanchis-Ojeda, R., Fabrycky, D. C., Winn, J. N., et al. 2012, Natur, 487, 449
Schmitt, J. R., Agol, E., Deck, K. M., et al. 2014, ApJ, 795, 167
Schwarz, G. 1978, AnSta, 6, 461
Shabram, M., Demory, B.-O., Cisewski, J., Ford, E. B., & Rogers, L. 2016, ApJ, 820, 93
Shen, Y., & Turner, E. L. 2008, ApJ, 685, 553
Silverman, B. W. 1986, Density Estimation for Statistics and Data Analysis (Boca Raton, FL: CRC Press)
Sinukoff, E., Howard, A. W., Petigura, E. A., et al. 2016, ApJ, 827, 78
Steffen, J. H. 2016, MNRAS, 457, 4384
Steffen, J. H., Fabrycky, D. C., Agol, E., et al. 2013, MNRAS, 428, 1077
Van Eylen, V., & Albrecht, S. 2015, ApJ, 808, 126
Vanderburg, A., Montet, B. T., Johnson, J. A., et al. 2015, ApJ, 800, 59
Weiss, L. M., & Marcy, G. W. 2014, ApJL, 783, L6
Weiss, L. M., Marcy, G. W., Rowe, J. F., et al. 2013, ApJ, 768, 14
Wright, J. T., Fakhouri, O., Marcy, G. W., et al. 2011, PASP, 123, 412
Wu, Y., & Lithwick, Y. 2013, ApJ, 772, 74
Xie, J.-W., Dong, S., Zhu, Z., et al. 2016, PNAS, 113, 11431
Zakamska, N. L., Pan, M., & Ford, E. B. 2011, MNRAS, 410, 1895